

One-dimensional turbulence modeling for cylindrical and spherical flows: Model formulation and application

David O. Lignell · Victoria B. Lansinger · Juan Medina · Marten Klein · Alan R. Kerstein · Heiko Schmidt · Marco Fistler · Michael Oevermann

Received: date / Accepted: date

Abstract The one-dimensional turbulence (ODT) model resolves a full range of time and length scales and is computationally efficient. ODT has been applied to a wide range of complex multi-scale flows, such as turbulent combustion. Previous ODT comparisons to experimental data have focused mainly on planar flows. Applications to cylindrical flows, such as round jets, have been based on rough analogies, e.g., by exploiting the fortuitous consistency of the similarity scalings of temporally developing planar jets and spatially developing round jets. To obtain a more systematic treatment, a new formulation of the ODT model in cylindrical and spherical coordinates is presented here. The model is written in terms of a geometric factor so that planar, cylindrical, and spherical configurations are represented in the same way. Temporal and spatial versions of the model are presented. A Lagrangian finite-volume implementation is used with a dynamically adaptive mesh. The adaptive mesh facilitates the implementation of cylindrical and spherical versions of the triplet map, which is used to model turbulent advection (eddy events) in the one-dimensional flow coordinate. In cylindrical and spherical coordinates, geometric stretching of the three triplet map images occurs due to the radial dependence of volume, with the stretching being strongest near the centerline. Two triplet map variants, TMA and TMB are presented. In TMA, the three map images have the same volume, but different radial segment lengths. In TMB, the three map images have the same radial segment lengths, but different segment volumes. Cylindrical results are presented for temporal pipe flow, a spatial nonreacting jet, and a spatial nonreacting jet flame. These results compare very well to direct numerical simulation (DNS) for the pipe flow, and to experimental data for the jets. The nonreacting jet treatment over-predicts velocity fluctuations near the centerline, due to the geometric stretching of the triplet maps and its effect on the eddy event rate distribution. TMB performs better than TMA. A hybrid planar-TMB (PTMB) approach is also presented, which further improves the results. TMA, TMB, and PTMB are nearly identical in the pipe flow where the key dynamics occur near the wall away from the centerline. The jet flame illustrates effects of variable density and viscosity, including dilatational effects.

Keywords One-dimensional turbulence · ODT · cylindrical · turbulence modeling

1 Introduction

The one-dimensional turbulence (ODT) model was introduced by Kerstein in 1999 [23]. ODT is computationally efficient because it only resolves flows in a single dimension. Turbulent advection is modeled through stochastic processes that are implemented by mapping functions on the domain using triplet maps.

D. O. Lignell · V. B. Lansinger
Department of Chemical Engineering, Brigham Young University, Provo, UT 84602
Tel.: 801-422-1772
E-mail: davidlignell@byu.edu

J. Medina · M. Klein · H. Schmidt
Brandenburgische Technische Universität Cottbus-Senftenberg, Germany

A. R. Kerstein
72 Lomitas Road, Danville, CA, USA

M. Fistler · M. Oevermann
Chalmers University, Gothenburg, Sweden

In ODT, the terms “eddy event” and “eddies” are historically used to denote these stochastic mapping processes. Eddy events occur concurrently with the solution of unsteady one-dimensional transport equations for momentum and other scalar quantities. Eddy event locations, sizes, and occurrence rates are specified dynamically and locally using the momentum fields that evolve with the flow. (Temperature fields or scalar fields are also used for buoyant flows.) Because the model is one-dimensional, it is limited to homogeneous or boundary layer flows, such as jets, wakes, mixing layers, and channel flows. These flows, however, are extremely common in turbulence research.

While ODT does not replace other turbulent simulation approaches, such as LES or DNS, the computational efficiency of ODT, combined with its resolution of a full range of scales, make it a useful tool that complements traditional simulation tools. For example, LES resolves large-scale turbulent structures but models subgrid scale processes. Such modeling, e.g., for reacting flows, is often done in a chemical state space [9]. In contrast, ODT resolves (in one dimension) fine scale diffusive and reactive structures in the natural physical coordinate (like DNS) but models large-scale advection.

ODT has been applied by a number of researchers to a wide range of flows. Early applications focused on configurations such as homogeneous turbulence, wakes, and mixing layers [23,25], and utilized only a single velocity component. Wunsch and Kerstein [54] studied layer formation in stratified flow. They added buoyant forcing effects to the shear forces normally used to specify ODT eddy rates. A kernel function K (with a coefficient c) was added to the triplet mapped velocity field to enable potential-kinetic energy exchange. Kerstein et al. [24] generalized this use of a kernel function and extended ODT to a vector formulation in which three velocity components are transported, with energy transfers among the components reflecting pressure-scrambling and return-to-isotropy phenomena. Ashurst and Kerstein [2] extended this approach to variable density flows, where an additional kernel J (with coefficient b) was added to triplet mapped velocity components to ensure conservation of both momentum and energy in variable density flows. These researchers also presented the formal “spatial” formulation of ODT in which the simulation is advanced in a downstream spatial coordinate rather than in time, as is done in the “temporal” ODT formulation. These advancements have facilitated ODT’s application to more complex flows, including combustion in jets [10,15,16,43,34,32,21] and fires [17,18,49,45,39], particle flows [46,52,14,51], and subgrid modeling for LES [5,48,47].

All of these simulated flows (and others not cited) used the planar formulation of ODT, even when comparing to experiments of cylindrical configurations. This comparison is reasonable for round jets because the Reynolds number is axially invariant in both constant-property spatial round jets and constant-property temporal planar jets [51]. To compare temporal ODT simulations to spatial experimental simulations, however, time on the ODT line must be converted to experimental axial spatial locations. This is normally done using a mean line velocity (such as the ratio of the integrated momentum flux to the integrated mass flux) [51], but this implies that all fluid parcels on the line have the same axial location time history. This assumption is not ideal for phenomena that are sensitive to time history, such as soot formation, flame extinction and reignition processes, and particle-turbulence interactions.

These limitations in applying the planar ODT formulation to cylindrical flows motivate the work presented here. In this paper, we extend the ODT model from the planar formulation to cylindrical and spherical formulations. There have been some previous efforts to implement cylindrical and spherical ODT formulations. Krishnamoorthy [27] implemented a cylindrical ODT formulation and applied the model in pipe and jet configurations. Lackmann et al. [28] implemented a spherical formulation of the linear eddy model (LEM) for engine applications. Here, we give a detailed description of cylindrical and spherical formulations of ODT. While the spherical formulation is included for completeness, we focus on the cylindrical formulation because it is most directly applicable to current and previous ODT research efforts. We defer to the literature for much of the existing ODT model formulation, e.g., [2,24,33], and focus on the new cylindrical and spherical geometries. For completeness, however, we include a summary of the ODT model formulation. We present results for the cylindrical formulation applied to a pipe flow, a round nonreacting spatial jet, and a round jet flame. A more detailed study of pipe flow than is possible in this paper is presented by Medina et al. [36]. Nevertheless, pipe flow is revisited in the present study because it is a useful case for exhibiting the effects of some of the refinements of the cylindrical formulation that are introduced here.

2 Cylindrical and spherical ODT formulations

Since we are emphasizing the model for cylindrical flows in this paper, we will only refer to the cylindrical formulation, while the spherical formulation is implied. Physically important spherical flows occur in

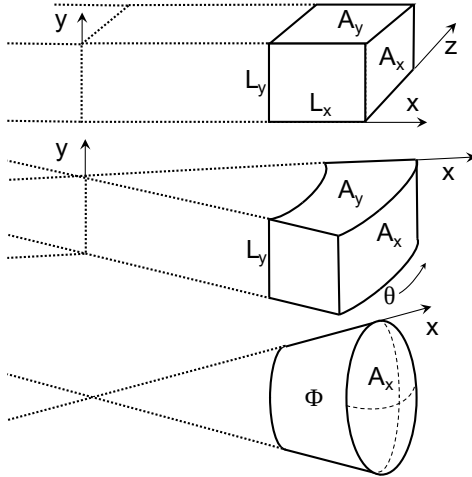


Fig. 1 Schematic diagram of cell volumes for planar (top), cylindrical (middle), and spherical (bottom) formulations.

geophysical and astrophysical fluid dynamics, including flows in planets and stars, e.g., spherical Rayleigh-Benard convection [12].

The new formulation affects the two primary aspects of the ODT model: (i) the specification of the eddy events through triplet maps and (ii) the one-dimensional evolution equations for transported quantities. Since ODT models turbulent advection solely through the eddy events, the evolution of the transport equations amounts to the solution of unsteady, one-dimensional partial differential equations that include diffusive and source terms. The sequencing of these operations during ODT advancement is described in Appendix A.

In the following, we will take x to be the line-oriented direction, while y and z are off-line directions. For planar and cylindrical geometries, y is taken to be the streamwise and axial directions, respectively. For cylindrical and spherical geometries, we will take x to be negative left of the origin and positive right of the origin.

We present the ODT model in terms of a discrete finite-volume formulation with grid cells (control volumes) defined by their face locations and cell positions located midway between the faces. For consistency with [33], we will refer to the left and right cell face locations as west and east, with subscripts e and w , respectively. Considering discrete grid cells also facilitates the description of the eddy events in the next section. Fig. 1 shows schematic diagrams of control volumes for the three geometries considered. A_x and A_y are the face areas perpendicular to the x and y directions, respectively; lengths L_x and L_y are also shown. In cylindrical and spherical configurations, the domain is interpreted as double wedges or double cones of arbitrary angle θ or solid angle Φ , respectively. Note that x and r are synonymous. (In the spherical case shown in the figure, the radial coordinate is shown, but the two angular coordinates are not explicitly shown.) For positive cell faces located at $x_{f,e}$ and $x_{f,w}$, the cell volumes for planar, cylindrical, and spherical configurations are $V_p = \frac{L_y L_z}{1} (x_{f,e} - x_{f,w})$, $V_c = \frac{L_y \theta}{2} (x_{f,e}^2 - x_{f,w}^2)$, and $V_s = \frac{\Phi}{3} (x_{f,e}^3 - x_{f,w}^3)$. When defining volumes on the one-dimensional domain, we can use arbitrary cell side lengths L_y and L_z in the y and z directions, as well as arbitrary angle θ and solid angle Φ . These quantities are ultimately normalized out of the formulation and results since ODT outputs and time advanced properties are intensive quantities. In general, we have

$$V = \begin{cases} \frac{1}{c} (x_{f,e}^c - x_{f,w}^c) & \text{if } x_{f,w} \geq 0, \\ \frac{1}{c} (|x_{f,w}|^c - |x_{f,e}|^c) & \text{if } x_{f,e} \leq 0, \\ \frac{1}{c} (|x_{f,w}|^c + x_{f,e}^c) & \text{if } x_{f,w} < 0 < x_{f,e}, \end{cases} \quad (1)$$

where c is 1, 2, or 3, for planar, cylindrical, and spherical, respectively. For the second case in Eq. 1, for negative $x_{f,e}$, the positions of $x_{f,e}$ and $x_{f,w}$ are reversed due to symmetry about the origin. The third case corresponds to a cell that contains the origin, in which case the volume is the sum of the wedge (or cone) volumes on either side of the origin.

In planar and cylindrical geometries, the areas A_y in Fig. 1 are their respective volumes divided by L_y . For a positive face position x_f , the face areas A_x are given by $L_y L_z$, $L_y \theta x_f = L_y \theta r$, and $\Phi x_f^2 = \Phi r^2$ for

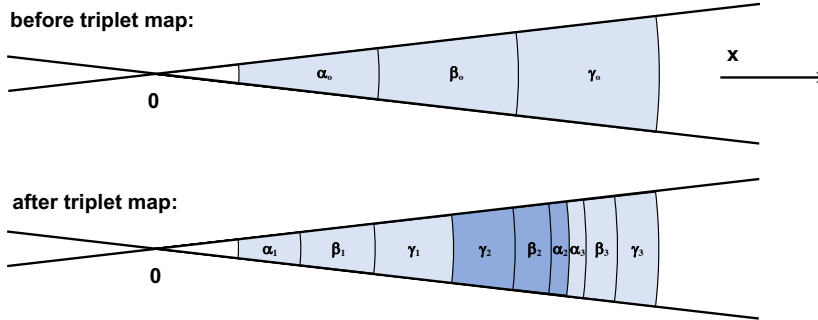


Fig. 2 Schematic diagram of a cylindrical triplet map. The map region is shaded. There are three grid cells before the triplet map, and nine cells after. After the triplet map, the three map images are separately shaded; each image of a given pre-map cell has the same volume (one-third the original volume). The nine final cells are labeled by the cells from which they originate.

planar, cylindrical, and spherical, respectively. In general, for arbitrary L_y , L_z , θ , and Φ , we take

$$A_x = |x_f|^{c-1}. \quad (2)$$

2.1 Eddy events

2.1.1 Triplet map A (TMA)

In the planar formulation of ODT, turbulent advection is modeled using stochastic, instantaneous eddy events. Within an eddy event, advection is implemented using the so-called triplet map [22]. (Other operations performed during an eddy event are discussed in Sec. 2.2.)

The triplet map is defined as follows. A region of the domain is selected such that $x_0 \leq x \leq x_0 + l$, where x_0 is the location of the left edge of the eddy and l is the eddy size. For a given scalar profile in the eddy region (such as a momentum component), three images of the profile are made. Each profile is compressed spatially by a factor of three and lined up along the domain in the eddy region. The middle copy is then spatially inverted (mirrored). This is applied to all transported properties. The triplet map is strictly conservative of all quantities and their statistical moments, and property profiles (though not property gradients) remain continuous. The triplet map increases scalar gradients and decreases length scales consistent with the effects of turbulent eddies in real flows. The maps are also local in the sense that scales decrease by a factor of three. Subsequent eddies in the same region will further decrease the scales by this factor, resulting in a cascade of scales. Eddy rates depend on the eddy size and the local kinetic energy field such that the eddy events follow turbulent cascade scaling laws.

For cylindrical and spherical flows, the triplet map formulation is modified. This can be done in several ways. In the first approach, here denoted TMA, we proceed similarly to the planar case, but rather than split the eddy region into thirds by distance, we split the eddy region into thirds by volume. These are equivalent for the planar case, but not in the cylindrical or spherical cases.

Fig. 2 is a schematic of a cylindrical eddy in the right half of the domain. The triplet-map region initially contains three cells labeled α_0 , β_0 , and γ_0 . The post-triplet-map state has three images of the original profile (three copies of the original three cells), and each image (and each cell within) has one-third of its original volume. Note the spatial inversion of the middle image.

The triplet map is implemented by specifying its effects on the cell locations and the cell contents. Before the map, the volume of each cell is recorded. The number of cells in the eddy region is tripled during the map, facilitated by an adaptive grid [33]. The locations of the edges of the eddy are unchanged by the map. The new interior cell face positions can then be computed sequentially from one edge of the eddy to the other. For example, we can march eastward from the west edge using the solution of Eq. (1) for the location $x_{f,e}$ of the east face of each successive cell, namely

$$x_{f,e} = \begin{cases} (x_{f,w}^c + cF_V V)^{1/c} & \text{if } x_{f,w} \geq 0, \\ -(|x_{f,w}|^c - cF_V V)^{1/c} & \text{if } x_{f,w} \leq 0, \\ (-|x_{f,w}|^c + cF_V V)^{1/c} & \text{if } x_{f,w} < 0 < x_{f,e}. \end{cases} \quad (3)$$

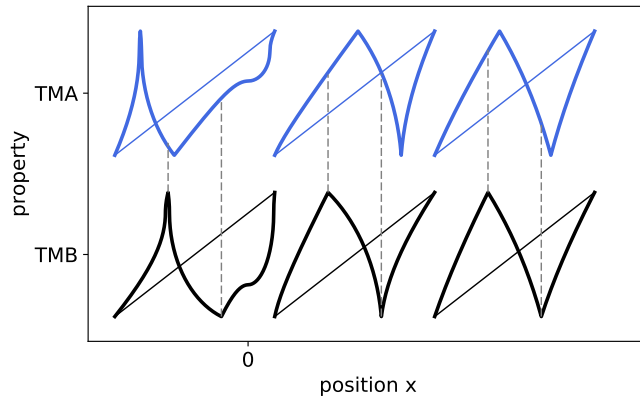


Fig. 3 Illustration of the effects of versions TMA and TMB of the cylindrical triplet map on the originally linear profile connecting the ends of each curve. Thick curves are mapped property profiles. Vertical dashed lines mark the radial 1/3 and 2/3 positions of the maps.

Here, F_V is a fractional multiplier of the volume under the triplet map ($F_V = 1/3$ for TMA). Note that, while shown in Fig. 2 for simplicity, the initial radial (x) intervals of cells α_0 , β_0 , and γ_0 do not need to be equal. Also, the edges of the triplet map do not normally coincide with cell faces; in that case, only the portion of a cell contained within the triplet map region is modified by the map. In Fig. 2, the interior cells α and γ after the triplet map would have one-third the volume of the portion of the respective original cell that was within the map region.

Some additional algebraic complexity arises if an eddy edge or a boundary between post-map images is contained within the interior of a cell. Indeed, these locations do not typically coincide with cell faces. Conceptually, this is handled by assuming the insertion of virtual cell faces at the eddy edges and image boundaries, which reduces these cases to the treatment that has been described.

Relative to the planar case, the cylindrical triplet map tends to stretch profiles nearer to the origin and compress profiles farther from the origin since the volume per unit radial distance is larger at higher radial distance (see Fig. 3 below).

2.1.2 Triplet map B (TMB)

An alternative triplet map, denoted TMB, is also considered. Rather than define the three images on an equal volume basis, the three images are defined on an equal radial interval basis. The volume fraction of each image is then computed using the volume-position relations in Eq. (1), where the positions x_f are the eddy edges, or the 1/3 or 2/3 image boundaries, and the image volume fractions F_V are then outputs rather than inputs. Using TMA, the volume fractions of the three images were each 1/3. TMB is implemented in much the same way as TMA, but the cell volume V in Eq. (3) is multiplied by the appropriate volume fraction F_V for the given image that the cell is mapped to rather than 1/3. Conservation is maintained since the volume fractions of the three images in TMB sum to unity.

A schematic of the action of TMA is shown in Fig. 2, where, for the β cells (for example), $V_{\beta_1} = V_{\beta_2} = V_{\beta_3} = V_{\beta_0}/3$. For both TMA- and TMB-type triplet maps we have $V_{\beta_1} + V_{\beta_2} + V_{\beta_3} = V_{\beta_0}$. However, for a TMB-type map, V_{β_1} volume in Fig. 2 would be smaller than V_{β_2} , and V_{β_3} because the left image would have a smaller outer radius.

Figure 3 illustrates the effect of TMA and TMB on initially linear profiles in a cylindrical configuration. Three maps TMA and TMB are shown at three radial locations. The vertical dashed lines are guidelines indicating the interior 1/3 and 2/3 positions of the maps. Note that these positions coincide with the high and low peaks for TMB, but not for TMA. Compare the left and right image of the middle TMA and TMB maps in Fig. 3. The left image of TMB is narrower (radially) than in TMA, and the right image of TMB is wider (radially) than in TMA; the resulting cell volumes in the left image of TMB are smaller than in TMA, and cell volumes in the right image of TMB are larger than in TMA. The stretching of TMA in reference to the location of the peaks relative to the 1/3 and 2/3 positions becomes less significant with increasing distance from the origin.

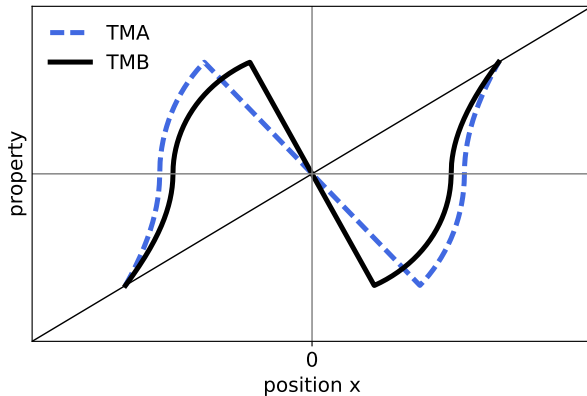


Fig. 4 TMA and TMB for maps centered on the origin for initially linear property profiles.

Both TMA and TMB exhibit nonlinear profiles within each of the three map images in Fig. 3. In this discussion, the nonlinearity occurs in relation to the initially linear profiles, which are used to illustrate a simple case. In general, the initial profile will be arbitrary. For planar flows, the three images are linearly compressed images of the initial profile; TMA and TMB result in identical mappings. In cylindrical and spherical flows, the three images exhibit some geometric distortion, as exhibited in Fig. 3. TMB reduces the geometric stretching compared to TMA in the sense that the three map images in Fig. 3 each have the same one-third radial segment lengths. The profiles within the segments are still stretched relative to a planar triplet map (whose image profiles would be linear in Fig. 3) and this is most notable near the origin at $x = 0$.

Figure 4 shows triplet maps centered on the origin for initially linear profiles for TMA and TMB. As expected, these maps are symmetric. Interestingly, the center image in each map preserves the linearity of the initial profile. This linearity is a consequence of the symmetry about the origin. In the center image, the (positive x or negative x) volume enclosed at any position is computed from Eq. (1) with $x_{f,i} = 0$. For example, for positive x , if a pre-map position is x_{pre} , the volume is $V_{pre} = \frac{1}{c}(x_{pre}^c - 0)$. The post-map volume is $F_V V_{pre}$, and the post-map position from Eq. (3) is $x_{post} = (0 + cF_V V_{pre})^{1/c} = F_V^{1/c} x_{pre}$, where F_V was defined above as the fraction applied to the volume for the given image ($F_v = 1/3$ for TMA). Hence, the post-map positions in the center image are proportional to the pre-map positions, resulting in a linear profile.

The center image through the origin in Fig. 4 is linear with nonzero slope as discussed above. This is in contrast to the post-map image through the origin shown in Fig. 3, where the profile at the origin has zero slope. This zero slope is due to the infinite compression there, which does not happen for the special case of Fig. 4. This flattening at $x = 0$ in Fig. 3 is a signature of the so-called “geometric lensing” effect, which is discussed further below.

2.2 Eddy selection and implementation

2.2.1 Eddy implementation

As explained in Sec. 2.1, advection is implemented within an eddy event using the triplet map. Additionally, ODT velocity component profiles are modified during the eddy event. This reflects the difference between flow evolution and scalar evolution. A conserved passive scalar, for example, is subject only to advection and diffusion. In ODT, molecular diffusion is advanced in time during the time intervals between eddy occurrences, as elaborated in Sec. 2.3 and Appendix A. Therefore, during an eddy event, conserved passive scalars and, more generally, properties other than velocity components, are subject only to the triplet map, but velocity profiles, as well as being triplet mapped, are subject to an additional modification. This reflects the fact that moment advancement involves pressure–gradient forcing (and possibly other body forcing) as well as advection and viscous transport, the latter of which is subsumed in the abovementioned treatment of molecular diffusion.

Unlike advection, which displaces fluid without changing its internal state, body forcing changes the fluid's internal state. This change can include quantities other than velocity; such effects are minor and therefore omitted for flow regimes considered here but included in a previous ODT formulation [20]. However, velocity profiles require modification during eddy events in order to enforce momentum and energy conservation in all situations and capture additional relevant phenomenology.

On this basis, the velocity change during an eddy event is symbolically denoted

$$u_i(x) \rightarrow u'_i(x) + c_i K(x) + b_i J(x). \quad (4)$$

Here and in the remainder of the model description, it is convenient to denote velocity components using subscripts. Pre-triplet map velocity components are denoted as $u_i(x)$, while $u'_i(x)$ and other primed quantities below refer to post-triplet map quantities. $K(x)$ and $J(x)$ are kernel functions, akin to wavelets, that are not uniquely prescribed by conservation laws. It is convenient to define $K(x)$ as the displacement of a point from its initial position by a triplet map and to let $J(x) = |K(x)|$. c_i and b_i are coefficients set by the constraint that momentum and energy are conserved, incorporating external sources and sinks where applicable.

For planar geometry, the definition of $K(x)$ specializes to [2,24]

$$K(x) = x - x_0 - \begin{cases} 3(x - x_0) & \text{if } x_0 \leq x \leq x_0 + \frac{1}{3}l, \\ 2l - 3(x - x_0) & \text{if } x_0 + \frac{1}{3}l \leq x \leq x_0 + \frac{2}{3}l, \\ 3(x - x_0) - 2l & \text{if } x_0 + \frac{2}{3}l \leq x \leq x_0 + l, \\ x - x_0 & \text{otherwise.} \end{cases} \quad (5)$$

In practice, $K(x)$ is evaluated from map-induced displacements of cell centers so that a single numerical procedure holds for all geometries (planar, cylindrical, and spherical) and both triplet map types (TMA and TMB).

Let Q_i denote the available eddy-integrated kinetic energy of component i ; in other words, Q_i is the maximum energy extractable by adding arbitrary multiples of the K and J kernels to the triplet-mapped component i velocity profile, subject to momentum conservation. The total available kinetic energy,

$$E_{kin} = \sum_i Q_i, \quad (6)$$

is a key input to the eddy selection process described in Sec. 2.2.2. E_{kin} is a natural basis for eddy selection because any coupling of the eddy to an external energy sink that exceeds E_{kin} should be energetically forbidden, thereby preventing eddy implementation.

Momentum conservation allows b_i in Eq. (4) to be expressed in terms of c_i and given quantities. To evaluate Q_i , the eddy-integrated kinetic energy is evaluated for $c_i = b_i = 0$ and for the value of c_i that minimizes the eddy-integrated kinetic energy. By definition, Q_i is the former minus the latter. Following [2], but using a more general notation applicable to the three coordinate systems used here, this gives

$$Q_i = \frac{P_i^2}{4S}, \quad (7)$$

where

$$P_i = u_{i,\rho K} - Au_{i,\rho J}, \quad (8)$$

$$S = \frac{1}{2}(A^2 + 1)\rho_{KK} - A\rho_{KJ}, \quad (9)$$

$$A = \frac{\rho_K}{\rho_J}, \quad (10)$$

$$\rho_K = \int_V \rho' K dV, \quad (11)$$

$$\rho_J = \int_V \rho' J dV, \quad (12)$$

$$\rho_{KK} = \int_V \rho' K^2 dV, \quad (13)$$

$$\rho_{KJ} = \int_V \rho' KJ dV, \quad (14)$$

$$u_{i,\rho K} = \int_V u'_i \rho' K dV, \quad (15)$$

$$u_{i,\rho J} = \int_V u'_i \rho' J dV. \quad (16)$$

All quantities in the integrands above depend only on x , and the indicated volume integration subsumes the x dependence of volume increments, as implied by specialization of Fig. 1 to infinitesimal x increments. The integrals are numerically implemented as sums over the grid cells in the eddy region, with dV replaced by cell volumes, evaluated using Eq. (1). The planar expressions in [2] are recovered by expressing dV as dx times a fixed value of the nominal cross-sectional area A_x shown in the top diagram of Fig. 1 and absorbing A_x into the definition of the density ρ .

As in [2], the cases considered here involve no external sources or sinks of energy or momentum, so conservation laws do not mandate nonzero values of c_i or b_i in Eq. 4. They are nevertheless assigned nonzero values in order to capture fundamental turbulence phenomenology that is central to the applications considered here, later illustrated by the case of turbulent pipe flow. In the present simulations, turbulent pipe flow is initialized with nonzero velocity only in the streamwise direction. For $c_i = b_i = 0$, the ODT pipe flow simulations would never produce nonzero velocities in the other directions or increase the energy content of those velocity components even if they were initially nonzero. The role of kernel application in this context is to enable the appropriate transfer of energy to those velocity components from the streamwise component, reflecting well-known pressure-scrambling and return-to-isotropy phenomenology.

Conservation laws and the plausible requirement that the mechanism of energy transfer among velocity components is invariant under relabeling of components [24] constrain the coefficients b_i and c_i such that they obey [2]

$$b_i = -c_i A, \quad (17)$$

$$c_i = \frac{1}{2S} \left(-P_i + \text{sgn}(P_i) \sqrt{(1 - \alpha)P_i^2 + \frac{\alpha}{2}(P_j^2 + P_k^2)} \right). \quad (18)$$

Additional modeling is needed to select the value of α within its allowed range $0 \leq \alpha \leq 1$. For this purpose, the tendency to recover isotropy is modeled here by requiring $Q_1 = Q_2 = Q_3$ upon the completion of an implemented eddy, which implies $\alpha = 2/3$. (Other choices of α likewise induce this tendency to varying degrees, and in some cases it is advantageous to choose a different value [24].)

2.2.2 Temporal formulation of eddy selection

The eddy selection process has been previously described in the literature [2,33,51]. Here, we provide a summary and some discussion related to the cylindrical and spherical implementations. The discussion here parallels that in [51].

Eddy events occur concurrently with the solution of the unsteady transport equations and are implemented instantaneously as triplet maps. Each eddy is parameterized by the position of its left edge x_0 and its size l . An eddy rate $\lambda_e(x_0, l)$ is associated with every possible eddy on the domain, and this rate is dependent on local momentum, density, and viscosity profiles on the line. The rate is taken to be $\lambda_e = \tau_e^{-1} l^{-2}$,

where τ_e is an eddy timescale, defined below. The rate of all eddies on the line is $\Lambda = \iint \lambda_e(x_0, l) dx_0 dl$. We can then form an eddy probability density function (PDF): $P(x_0, l) = \lambda_e(x_0, l) / \Lambda$.

In principle, eddy occurrence times can be sampled based on Poisson statistics with mean rate Λ where the corresponding eddy position x_0 and size l are sampled from $P(x_0, l)$. In practice, however, Λ and $P(x_0, l)$ are continually evolving, implying prohibitively expensive re-evaluations at each ODT evolution step that are exacerbated by an expensive numerical inversion required for each sampling from $P(x_0, l)$. Instead, an alternative sampling procedure is used, as described within a discussion of various details of ODT time advancement in Appendix A.

The eddy timescale τ_e is computed as in [2], and we extend the treatment to cylindrical and spherical flows. The equations below apply to the temporal ODT formulation, and modifications for the spatial ODT formulation follow in Sec. 2.2.3. τ_e is given by

$$\frac{1}{\tau_e} = C \sqrt{\frac{2}{\hat{\rho}_{KK} V_\epsilon l^2} \left(\frac{KK}{V_\epsilon l^2} E_{kin} - Z E_{vp} \right)}, \quad (19)$$

where E_{kin} is kinetic energy, V_ϵ is the eddy volume, and $KK = \int_V K^2 dV$.

The expression for τ_e in Eq. (19) follows from the scaling

$$E_{kin} \propto \frac{1}{2} m v^2 \propto \frac{1}{2} \rho V_\epsilon \frac{l^2}{\tau^2}. \quad (20)$$

For variable-density flows, ρ in Eq. (20) is replaced with $\hat{\rho}_{KK} = \rho_{KK} / KK$, which appears in Eq. (19). $\hat{\rho}_{KK}$ is a form of weighted density averaging that is motivated by a heuristic analogy between the triplet map and variable-density eddy kinematics [2]. Other factors in Eq. (19) follow previous conventions [3] and affect mainly the assignment of model parameters.

$Z E_{vp}$ is a viscous penalty that is subtracted from E_{kin} in Eq. (19). This term acts to suppress unphysically small eddies. The viscous penalty energy is given by

$$E_{vp} = \frac{V_\epsilon \bar{\mu}_\epsilon^2}{2l^2 \bar{\rho}_\epsilon}. \quad (21)$$

Here, $\bar{\rho}_\epsilon$, and $\bar{\mu}_\epsilon$ are eddy volume averages of density and dynamic viscosity, respectively. This follows from application of the scaling in Eq. (20) to E_{vp} followed by generalization to variable-property flows. To obtain an energy scale corresponding to the eddy motion that is marginally balanced by viscous damping, τ in Eq. (20) is taken to be $l^2/\nu = l^2\rho/\mu$, where ν and μ are the kinematic and dynamic viscosities. This value of τ corresponds to an eddy whose turnover time is comparable to the time required for viscous dissipation of the eddy motion.

Z is the viscous penalty model parameter, and C is the eddy rate model parameter. C and Z are adjustable parameters set by the user. Simulation results are sensitive to C since it directly scales the rate of turbulence evolution. Free shear flows, such as jets, wakes, and mixing layers, are generally insensitive to Z , but Z is important in near-wall flows, such as channel and pipe flows [48].

In order to suppress unphysically large eddies, which may occur in the eddy sampling procedure and adversely affect turbulent mixing, which is dominated by large eddies, a large-eddy suppression mechanism is often included. Several large eddy suppression models have been used [2, 10, 15]. For constrained flows, such as pipe or channel flows, a simple fraction of the domain length is sufficient. For free shear flows, such as jets, the elapsed time method is preferred, in which only eddies satisfying $t \geq \beta_{les} \tau_e$ are allowed, where β_{les} is a model parameter, and t is the current simulation time. In the spatial formulation, these times t and τ_e are replaced with lengths, as described in the next section.

2.2.3 Spatial formulation of eddy selection and implementation

The evolution equations for the spatial ODT formulation are presented in Sec. 2.4.1. Those equations have the form of steady-state parabolic boundary layer equations. The ODT line evolves downstream in a spatial coordinate rather than evolving in the time coordinate as is done in the temporal formulation. The spatial formulation applies to planar and cylindrical flows. In the temporal formulation, the integrals presented in Eqs. (11-16) are evaluated over the volume along the line. In the spatial formulation, dV is replaced by $v dA$, and the integrals are performed over area (A_y) along the line. v is the streamwise (off-line) velocity, and dA is a differential area in the plane perpendicular to the streamwise y direction. That is, integrals over dV versus $v dA$ represent volume versus volume rate integrations in the temporal and spatial formulations,

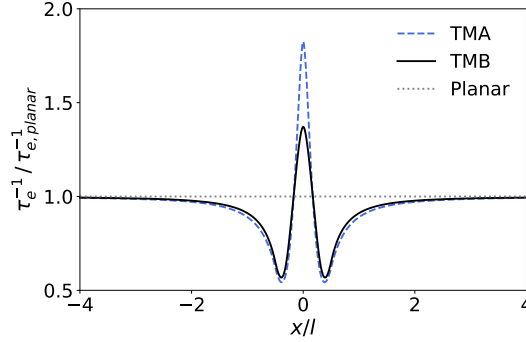


Fig. 5 Normalized inverse eddy timescale τ_e^{-1} versus normalized position for three triplet map variants based on linear velocity profiles in x .

respectively (see Sec. 2.4.1). E_{kin} in Eqs. (6, 19) has units of energy per time ($\text{kg m}^2 \text{s}^{-3}$) in the spatial formulation. In Eq. (21), V_ϵ is replaced with $\tilde{v}_\epsilon A_{y,\epsilon}$, where \tilde{v}_ϵ is the Favre averaged velocity in the eddy region and $A_{y,\epsilon}$ is the eddy area in the plane perpendicular to the streamwise direction. In doing this, we are replacing a measure of the mass $m = \bar{\rho}_\epsilon V_\epsilon$ in the eddy region with a measure of the mass flow rate $\dot{m} = \bar{\rho}_\epsilon A_{y,\epsilon} \tilde{v}_\epsilon$ in the eddy region.

In the spatial formulation, the line is advanced in the streamwise y coordinate rather than in time, so $1/\tau_\epsilon$ is divided by \tilde{v}_ϵ , giving it units of inverse length. Likewise, eddy sampling in the time advancement scheme described in Appendix A is converted into a spatially advancing treatment by replacing the eddy sampling time increment Δt_s in Eq. (44) by a spatial increment Δy_s . The eddy rate distribution is modified accordingly.

2.2.4 Eddy timescale profiles

Here we compare the eddy timescales in the temporal, planar, and cylindrical formulations. Figure 5 shows profiles of τ_e^{-1} (which is proportional to the eddy rate) for TMA, TMB, and a planar triplet map. In evaluating these profiles, τ_e^{-1} was computed at each point using an eddy of constant size l centered at the given point. A simple linear velocity profile is used, and the same profile is used in each eddy region at each evaluation point. In Fig. 5, τ_e^{-1} is constant for the planar map, and the cylindrical maps are normalized by this value. The domain is scaled by the eddy size used so that the scaled plot is independent of the eddy size. For TMA and TMB, τ_e^{-1} departs from the planar case within about two eddy sizes of the centerline. The departure is due to the geometric stretching of the cylindrical triplet maps, as noted in Figs. 2 and 3. The maps TMA and TMB have similar τ_e^{-1} profiles, but the central spike in the profile shown in Fig. 5 is significantly lower for TMB than for TMA.

The difference in τ_e^{-1} for the cylindrical and planar triplet maps suggests the use of a planar formulation for evaluating τ_e^{-1} in an otherwise cylindrical flow. While a planar formulation may be used for evaluating τ_e^{-1} , the actual implementation of the eddy would use the cylindrical formulation. This is possible because the evaluation of τ_e^{-1} is independent of the actual implementation of an eddy and the associated velocity redistribution through kernels. We proceed as follows. In the calculation of τ_e^{-1} at a given location y_0 with a given eddy size l , we make a copy of the ODT line that contains only the eddy region and the ODT variables needed for the τ_e^{-1} calculation (velocity components, density, and viscosity). We call this the eddy line and implement a planar eddy on the line; the K kernel is evaluated using its analytic form in Eq. (5). Finally, τ_e^{-1} is computed with all integrals performed assuming a planar geometry. If an eddy is accepted, then the eddy is implemented as a cylindrical eddy. That is, TMB (or TMA) is applied to the ODT line in the eddy region, kernel coefficients c_i and b_i are computed in a cylindrical geometry with cylindrical integrations, and the kernel contributions to the velocities are applied. In evaluating the kernel, Eq. (5) is again applied, although different versions could be used. For example, defining the kernel directly in terms of fluid particle displacement under the cylindrical triplet map could be done. This hybrid planar-TMB approach (PTMB) allows eddy selection based on a different timescale evaluation than for the implemented eddies. The difference would be of the magnitude shown in Fig. 5.

In summary, three triplet map approaches are considered in cylindrical and spherical flows for selection and implementation of eddy events: TMA, TMB, and PTMB. For TMA and TMB, the kernel is defined in terms of cell displacements. For PTMB, the kernel is defined as in Eq. (5). Results of these approaches are compared in Sec. 3.

2.3 Temporal evolution equations

This section summarizes the temporal evolution equations for transported quantities solved between eddy events. These equations represent a Lagrangian finite-volume formulation that is implemented in conjunction with an adaptive mesh. The Lagrangian formulation differs somewhat from standard Eulerian finite-volume approaches, notably in the form of the continuity equation and the absence of advective fluxes. The equations and a discussion of some of the subtleties related to the one-dimensional cylindrical and spherical formulations of ODT are given here.

continuity:

$$\rho V = \text{constant}, \quad (22)$$

species:

$$\frac{dY_k}{dt} = -\frac{j_{k,e}A_{x,e} - j_{k,w}A_{x,w}}{\rho V} + \frac{\dot{m}_k'''}{\rho}, \quad (23)$$

momentum:

$$\frac{du}{dt} = -\frac{\tau_{u,e}A_{x,e} - \tau_{u,w}A_{x,w}}{\rho V}, \quad (24)$$

$$\frac{dv}{dt} = -\frac{\tau_{v,e}A_{x,e} - \tau_{v,w}A_{x,w}}{\rho V} - \frac{1}{\rho} \frac{d\hat{P}}{dy} + \frac{(\rho - \rho_\infty)g}{\rho}, \quad (25)$$

$$\frac{dw}{dt} = -\frac{\tau_{w,e}A_{x,e} - \tau_{w,w}A_{x,w}}{\rho V}, \quad (26)$$

energy:

$$\frac{dh}{dt} = -\frac{q_e A_e - q_w A_w}{\rho V} + \frac{1}{\rho} \frac{dP}{dt}. \quad (27)$$

In these equations, V is a cell volume, A represents cell face areas, ρ is mass density, Y_k is mass fraction of species k , j_k is species mass flux, \dot{m}_k''' is the species mass source per unit volume, τ is viscous stress, and g is gravitational acceleration. Momentum components u_i are denoted u , v , and w here, and P is the thermodynamic pressure. For planar and cylindrical geometries, u refers to velocity in the line-oriented x direction, v is the streamwise velocity, and w is z -directed for planar geometries and nominally azimuthal for cylindrical geometries. There are no fully analogous interpretations in the spherical formulation. In the energy equation, h is enthalpy and q is heat flux.

Equations (22-27) were derived from the Reynolds Transport Theorem [6], which for some scalar per unit mass β is

$$\frac{d}{dt} \int_{\Omega} \rho \beta dV = \frac{d}{dt} \int_{\hat{\Omega}} \rho \beta dV + \int_{\hat{\Pi}} \rho \beta \mathbf{u}_R \cdot \mathbf{n} dA. \quad (28)$$

Here Ω is a Lagrangian system defined by a marked mass of fluid that can be total mass or the mass of a given species, and Π is its boundary surface. $\hat{\Omega}$ and $\hat{\Pi}$ refer to the control volume and surface coinciding with the system at a given instant. Also, \mathbf{n} is a unit normal vector pointing out of the boundary and \mathbf{u}_R is the relative velocity between system and control volume boundaries $\mathbf{u}_R = \mathbf{u}_\Pi - \mathbf{u}_{\hat{\Pi}}$. When applied to a grid cell control volume, assuming constant properties on cell faces and within the cell volume, Eq. (28) yields the following generic transport equation for β ,

$$\frac{d\beta}{dt} = -\frac{j_{\beta,e}A_{x,e} - j_{\beta,w}A_{x,w}}{\rho V} + \frac{S_\beta}{\rho V}, \quad (29)$$

where S_β is the Lagrangian source term from the conservation law for β (the term on the left-hand side of Eq. (28)), $j_\beta = \rho\beta u_{\beta,R}$ is the diffusion flux of β , and we have divided through by $\rho V = \text{constant}$, Eq. (22).

In the continuity equation, $\beta = 1$, $j_\beta = 0$, and $S_\beta = 0$. In species equations, $\beta = Y_k$ and $S_\beta = \int_\Omega \dot{m}_k''' dV$. In the momentum equations, $\beta = u_i$, $j_\beta = 0$, and $S_\beta = -\int_\Pi (\hat{P}\delta + \tau) \cdot \mathbf{n} dA + \int_\Omega (\rho - \rho_\infty) g dV$, where δ is the unit dyadic, and τ is the viscous stress tensor. In the energy equation, $\beta = \varepsilon = h - P/\rho$, $j_\beta = 0$, and $S_\beta = \dot{Q} + \dot{W} = -\int_\Pi \mathbf{q} \cdot \mathbf{n} dA - \int_\Pi P \mathbf{n} \cdot \mathbf{u}_\Pi dA$ from the first law of thermodynamics. These relations correspond to Eqs. (22-27) when integrated over the control volume, but they are also useful for describing the spatial evolution equations in cylindrical coordinates below.

In the Lagrangian formulation, the continuity equation reduces to a statement that the mass in any grid cell is constant. In constant density flows, the cell volume is constant, and there is no in-line dilatation. In flows with dilatation (e.g., flows with heat release), the cell volume changes in order to maintain constant mass in the cell. This constraint specifies the cell size but not the cell location. In a one-dimensional domain with a fixed boundary, the cell volume changes uniquely determine the displacements, and hence the locations, of all cells. Open domain flows like jets and mixing layers need special treatment. Planar flows are treated as in [33], in which the center of the expansion for any given time step is kept fixed so that there is equal volume expansion on either side of this expansion center. However, this is conceptually problematic for cylindrical and spherical ODT formulations due to the ‘‘geometric lensing’’ effect of x -dependent cell shape that magnifies displacements through the origin. (This was referenced above in Sec. 2.1.2.) For these flows, expansion or contraction occurs separately on either side of the origin; that is, the cell fluid at the origin is fixed.

Outflow due to expansion is treated by splitting any displaced cell that contains a domain boundary and then truncating the domain to discard regions outside the boundary. Inflow due to contraction is treated by expanding the boundary cell faces to the location of the domain boundary, which proportionately increases the mass in those cells for the given density. Alternatively, a new cell can be formed that extends to the domain boundary and uses boundary conditions to determine the cell property values. Further discussion for closed domains is given below.

In the momentum equations, Eqs. (24-26), ρ_∞ refers to the density of the ambient fluid in the buoyant source term. \hat{P} is a prescribed pressure field (if used), which is not a dynamic variable in the ODT model. (Note that compressible ODT formulations are possible and have been implemented [20, 43].) The pressure gradient source term is considered only in the streamwise direction. Viscous stresses τ are modeled as

$$\tau_u = -\mu \frac{du}{dx}, \quad \tau_v = -\mu \frac{dv}{dx}, \quad \tau_w = -\mu \frac{dw}{dx}, \quad (30)$$

where μ is the dynamic viscosity. These constitutive relations account only for the radial contribution to the stresses, which are assumed dominant.

Note that the velocity components u , v , and w are carried in ODT for the specification of the eddy events and as the model prediction of the flow field, but they are not advecting since advection processes are modeled through the eddy events.

In the energy equation, Eq. (27), only pressure work is included; kinetic energy and viscous dissipation are neglected. While not shown, energy source terms, such as from radiation, could be added. The pressure term in Eq. (27) arises in constant or constrained volume ideal gas flows (e.g., piston engines). This term is treated as in [33] and derived in Appendix B, with some extensions and minor corrections. The dP/dt term is not needed in the three simulations discussed in this paper.

While the continuity, species, momentum, and energy equations are shown above, and are common in ODT simulations, other transport equations may be included as needed. Examples include soot moments and mixture fraction transport equations.

2.4 Spatial formulation of cylindrical ODT

2.4.1 Governing equations

In the temporal formulation of ODT, the one-dimensional line evolves in a time coordinate. In the spatial formulation of ODT, which applies to 2D flows at steady state, the one-dimensional line evolves in a downstream spatial coordinate. Spatial ODT is applied to planar or cylindrical flows; there is no spatial analog for spherical flows. The evolution equations are parabolic boundary-layer equations that admit solution by a marching algorithm in the downstream coordinate using the same formulation as applies for marching in the time coordinate in the temporal formulation. In spatial ODT, the ODT line is in the

cross-stream direction for which gradients are high, and the evolution direction is streamwise. As usual for boundary-layer flows, we assume that axial transport is negligible relative to cross-stream transport. While the flow is assumed to be steady-state with respect to the evolution equations, instantaneous stochastic eddy events are still applied, as described in Sec. 2.2.3, and will differ for each flow realization. So despite the nominal steadiness of each flow realization, an ensemble of such realizations is analogous to an ensemble of instantaneous physical flow states with regard to the statistics that can be gathered, a consequent restriction being that time-history information is not available. In contrast, temporal ODT captures time-history information but provides a lower-dimensional representation of spatial structure.

The spatial formulation of ODT was described in [2, 33] for planar flows. The derivation for cylindrical flows is given here. In this derivation, we will use r in place of x for clarity. The Reynolds Transport Theorem Eq. (28) at steady state in terms of S_β is

$$S_\beta = \int_{\hat{\Omega}} \rho \beta \mathbf{u}_R \cdot \mathbf{n} dA. \quad (31)$$

The Gauss Divergence Theorem is applied and we write the volume integral over r , y , and θ . The integral over θ gives an arbitrary θ factor, and derivatives with respect to θ are zero. The y component of \mathbf{u}_R is v , and we use $j_\beta = \rho \beta u_R$, giving

$$S_\beta = \theta \int_y \int_r \frac{\partial(\rho \beta v)}{\partial y} r dr dy + \theta \int_y \int_r \frac{1}{r} \frac{\partial(j_\beta r)}{\partial r} r dr dy. \quad (32)$$

We differentiate this equation with respect to y , reflecting the parabolic nature of the flow in the y direction.

$$\frac{dS_\beta}{dy} = \theta \int_r \frac{\partial(\rho \beta v)}{\partial y} r dr + \theta \int_r \frac{1}{r} \frac{\partial(j_\beta r)}{\partial r} r dr. \quad (33)$$

This equation is multiplied by the factor L_y , the integrals appearing are performed over the region of a control volume, and the result, rewritten in terms of the cell volume and face areas, Eqs. (1,2), is

$$\frac{d(\rho \beta v V)}{dy} = -[j_{\beta,e} A_{r,e} - j_{\beta,w} A_{r,w}] + L_y \frac{dS_\beta}{dy}. \quad (34)$$

Refer also to Fig. 1. The continuity equation for spatial flows gives

$$\rho v V = \text{constant}. \quad (35)$$

Dividing Eq. (34) by $\rho v V$ gives

$$\frac{d\beta}{dy} = -\frac{j_{\beta,e} A_{r,e} - j_{\beta,w} A_{r,w}}{\rho v V} + \frac{L_y}{\rho v V} \frac{dS_\beta}{dy}. \quad (36)$$

This generic spatial equation is the analog of the temporal version in Eq. (29). Here, we use d/dy instead of d/dt , and the RHS has an extra factor of $1/v$. The source term $L_y dS_\beta/dy$ can be replaced with the source terms for species, momentum, and energy given above. In those source terms, d/dy collapses the y components of volume or area integrals in S_β , but those y components are recovered with the L_y factor.

v is nonuniform on the line, and its value implies the local residence time for a given parabolic streamwise advancement. Importantly, the streamwise velocity in the denominators of the terms in Eq. (36) requires that v always be nonzero and positive. This restriction is due to the parabolic boundary-layer equations being mathematically inconsistent for negative v . This was discussed in [2], where it was noted that the addition of the kernels to the velocity during a triplet map in Eq. (4) can result in negative v . This effect is mitigated by simply using $c_i = b_i = 0$ in Eq. (4) in instances that would otherwise result in negative v .

2.4.2 Solution approaches

The temporal or spatial evolution equations are ordinary differential equations (ODEs) at each grid cell. Three solvers are implemented: a first-order explicit Euler method, a first-order semi-implicit method used for treating stiff chemistry, and a second-order Strang splitting method [50] also used for stiff chemistry. The semi-implicit method uses CVODE [8] to advance the coupled ODEs in a given cell. Each cell is integrated sequentially. Chemical source terms are treated implicitly, while mixing terms are treated explicitly and are fixed at the values at the beginning of the step.

Continuity is imposed as follows. We focus here on reacting gas flows with variable temperature, composition, and density. In the temporal formulation, the cell sizes Δx_o and densities ρ_o are recorded before each advancement step. The temporal evolution ODEs are then advanced one step. Temperature is computed from the thermodynamic state, and density ρ_f is then computed from the ideal gas law. The cell sizes at the end of the step are then calculated by imposing continuity: $\Delta x_f = \rho_o \Delta x_o / \rho_f$. Cell face positions are then computed using Δx_f as previously described in Sec. 2.3. The spatial formulation treatment is similar, but the pre-step velocity v_o is also recorded, and Eq. (35), $\Delta x_f = \rho_o v_o \Delta x_o / (\rho_f v_f)$, is used, where v_f is the post-step velocity computed from the momentum equation.

For all solution approaches, the system of ODEs in each grid cell is advanced with a step size set below the diffusive stability limit, computed as the smallest step required for all ODEs over all grid cells.

2.5 Discussion

The finite-volume form of these equations is convenient for solution. The equations are well-behaved at all grid positions in planar, cylindrical, and spherical geometries. This contrasts the differential form of the equations, which have singularities that require special treatment at the origin for cylindrical and spherical geometries due to division by the local radial position.

Here, the only issue is that cell face areas decrease to zero as we approach the origin. As a result, transport across that face tends toward zero, effectively decoupling the two halves of the domain. For cell faces at or very close to the origin, a zero flux boundary condition is implied. (Technically, the unsteady flux can be nonzero but since it multiplies a zero area, the flow is also zero.) This can result in zero gradients with discontinuous profiles at the origin.

This effect is corrected during mesh management operations by ensuring that the origin is nearly in the center of the cell containing it so that the flows through either side of that cell are not artificially imbalanced due to the face locations. In any case, eddy-induced transport across the origin under the turbulent conditions of interest are far greater than molecular-diffusive fluxes, so there is no significant barrier to transport across the origin irrespective of diffusive transport mitigation procedures.

One subtlety in the cylindrical and spherical formulations is that the equations include only one-dimensional, line-oriented transport. However, the formulation is nominally axisymmetric; hence solution on both sides of zero seems redundant. This would be true if we were only solving the evolution equations. The addition of the eddy events breaks the symmetry. We model a turbulent flow with instantaneous asymmetry and eddies that can cross the centerline. The evolution equations can then be thought of as prescribing distinct but coupled time histories of radial property profiles for positive and negative x (radius r), respectively.

3 Results

This section presents results for three demonstration cases of the cylindrical ODT formulation: a temporal pipe flow, a round spatial jet, and a round spatial jet flame. Mesh resolution is performed as discussed at length in [33]. Grid density factors (defined in [33]) of 30 and 80 were used for the jet cases and the pipe flow cases, respectively. Grid resolution studies that were performed gave results that were grid-independent. The smallest cell size used in the round jet and jet flame cases were 20 μm , and 64 μm , respectively. Pipe flow simulations are performed with $(\Delta r^+)_{min} = 0.333$. Time step sizes for the jets and pipe simulations are 0.2 and 0.5, respectively, multiplied by the diffusive stability limit $\frac{1}{2}(\Delta x^2/\Gamma)_{min}$, where Γ the diffusivity of a given transported scalar.

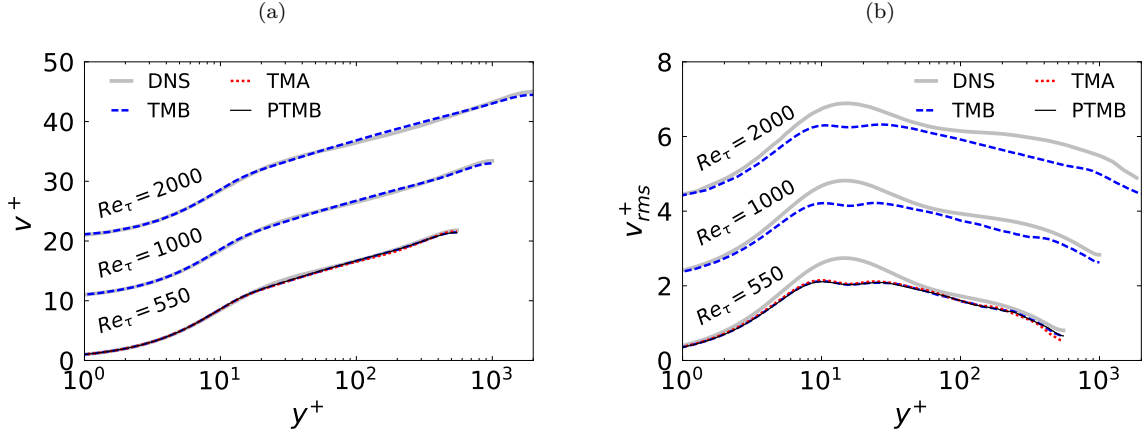


Fig. 6 ODT simulations and DNS experiments of streamwise mean (a) and RMS (b) velocity profiles at three Reynolds numbers. Cases TMA and PTMB are only shown for $Re_\tau = 550$.

3.1 Pipe flow

We present results for incompressible pipe flow simulations using the temporal, cylindrical ODT formulation. Results for three different friction Reynolds numbers $Re_\tau = 550, 1,000, 2,000$ are compared to DNS results from Khoury et al. [26] ($Re_\tau = 550, 1,000$) and Chin et al. [7] ($Re_\tau = 2,000$). Simulation results were produced using a pipe diameter of $D = 2.0$ m and flow density of 1.0 kg m^{-3} . For fully developed pipe flow, it is possible to estimate the value of a constant mean pressure gradient driving the flow based on the value of the friction velocity, the pipe radius and the density. Friction velocity values of 1 ($Re_\tau = 550, 1,000$) and 2 m s^{-1} ($Re_\tau = 2,000$) were assumed and used to calculate the mean pressure gradient driving the flow. Simulation results achieving statistical convergence for the friction velocity were verified afterwards as a check on the input parameters. The simulations used initial conditions with constant velocity profiles. The simulations were run to a developed flow state, after which simulation data were gathered until statistical convergence for the root mean square (RMS) velocity difference from the mean profiles occurred. The total normalized run time $t_{run}/\tau_{pipe} = t_{run}\bar{u}/D$ was 20,200, 25,070, and 28,140 for $Re_\tau = 550, 1,000$, and 2,000, respectively, where \bar{u} is the average velocity and D is the pipe diameter.

The simulations were performed with parameters of $C = 5$ and $Z = 350$ for the temporal ODT formulation. Additionally, a restriction was imposed on the eddy size range by selecting eddies only up to a maximum normalized size of $L_{e,max}/D = 1/3$. This restriction limits the eddy size by construction, as opposed to the large-eddy suppression mechanism commonly used in ODT simulations [27, 48]. The values of C , Z , and $L_{e,max}/D$ were adjusted to give good agreement of the ODT results compared to the DNS. Schmidt et al. [48] showed that higher Z results in the buffer-layer being located further from the wall; increasing C results in a lower slope of the mean streamwise velocity in the log-layer; and higher $L_{e,max}/D$ gives a smaller mean streamwise velocity in the wake region.

Figure 6(a) results of the mean streamwise velocity profiles in wall units for each of the three Re_τ considered. The profiles are shifted vertically by 10 and 20 units in the figure for presentation. The $Re_\tau = 550$ case shows a comparison of the TMA, TMB and the hybrid planar/cylindrical approach of the TMB eddy event implementation (PTMB). As seen in the figure, the differences between TMA, TMB, and PTMB are negligible, and so were not considered for the higher Re_τ cases. The agreement between the ODT and DNS for the mean velocity is excellent for all three Re_τ values.

Figure 6(b) shows the streamwise root mean square (RMS) velocity profiles for each Re_τ . These profiles are shifted vertically by 2 and 4 units in the figure for presentation. The ODT RMS velocity profiles deviate from the DNS more strongly than the mean velocity profiles, with the ODT value at the peak approximately 20% lower than the DNS. The qualitative shape of the profiles, however, is the same as expected from previous ODT channel flow simulations performed with the planar formulation [38, 33]. The small double peak structure of the ODT was described in [33] and arises from alignment of the triplet map images in the near-wall region. The slight depression between the ODT peaks aligns with the DNS peak, resulting in a larger difference between the RMS profiles than an extrapolation of the surrounding ODT

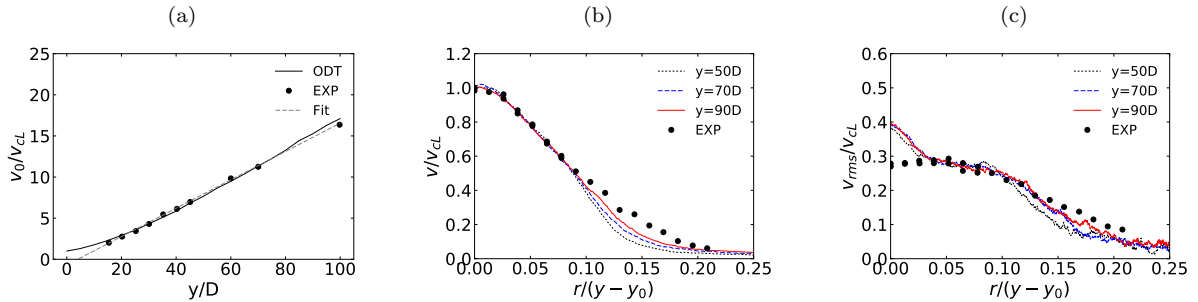


Fig. 7 Round jet results for TMB: (a) mean axial velocity along the centerline versus downstream location; (b) radial profiles of mean axial velocity at three downstream locations; (c) root mean square (RMS) radial profiles of streamwise velocity at three downstream locations.

profiles to the peak region would give. As for the mean profiles, the differences between TMA, TMB, and PTMB for the RMS velocity profiles are negligible. Small differences appear only for the RMS profiles near the centerline. We expect this because of the eddy timescale behavior seen in Fig. 5

A more complete ODT analysis of turbulent pipe and channel flows in both temporal and spatial formulations, including turbulent kinetic energy budgets, is presented in [36].

3.2 Round jet

The new cylindrical ODT formulation is demonstrated in a nonreacting round turbulent jet. Results are compared to the experimental data of Hussein et al. [19]. The jet consists of air issuing into air through a 1 in (0.0254 m) diameter duct. The jet exit velocity is 56.2 m s^{-1} and is well-approximated by a top-hat profile. The reported Reynolds number is 95,500, where $Re = Dv_0/\nu$, and D is the jet exit diameter, v_0 is the jet exit velocity, and ν is the kinematic viscosity. The ODT simulations use the same diameter and velocity, but a kinematic viscosity of $1.534 \times 10^{-5} \text{ m}^2 \text{ s}^{-1}$, giving a Reynolds number of 93,056. The initial velocity profile in the ODT simulations is a modified top-hat profile in which a hyperbolic tangent function of width $\delta = 0.1D$ is used on either side of the jet to smooth the transition between the jet and the free stream:

$$v(x) = v_{min} + \Delta v \cdot \frac{1}{2} \left(1 + \tanh \left(\frac{2}{\delta} (x - x_{c1}) \right) \right) \cdot \frac{1}{2} \left(1 + \tanh \left(\frac{2}{\delta} (x_{c2} - x) \right) \right). \quad (37)$$

Here, x_{c1} and x_{c2} are the center locations of the tanh transition, $-D/2$ and $D/2$, respectively. In the spatial formulation of ODT, the streamwise velocity must be positive everywhere on the line due to v in the denominator on the right hand side of the evolution equations (see Sec. 2.4.1). As such, a small $v_{min} = 0.1 \text{ m s}^{-1}$ is added uniformly to the velocity profile. Δv is taken to be the jet velocity of 56.2 m s^{-1} .

ODT simulations were performed using the TMB triplet map with parameters $C = 5.25$, $\beta_{les} = 3.5$, and $Z = 400$. The value of Z is the same as the spatial simulations in [39] and was not adjusted. The values of C and β_{les} were adjusted to give good agreement of the jet evolution with the experimental data. Note the very close agreement of the C and Z parameters here to the optimal values used for the pipe flow simulations where $C = 5$ and $Z = 350$. This illustrates a level of robustness in the ODT parameters between the two configurations and suggests that intermediate values could be successfully applied in both configurations. The pipe flow is sensitive to Z , as noted above, but the jet is not, so $Z = 350$ would be preferred. Figure 7 shows results of the simulations. Here, 1024 independent ODT realizations were performed and results were ensemble averaged. All quantities are normalized consistent with jet similarity scaling. Downstream locations are normalized by the jet diameter D , and radial locations are normalized by $(y - y_0)$ where y is the downstream location and $y_0 = 4D$ is the virtual origin used in [19]. In the figure, v_0 is the jet exit velocity and v_{cL} is the local mean axial centerline velocity. Here, r is used to denote both the experimental radial location and the ODT line position x .

Figure 7(a) shows v_0/v_{cL} versus y/D ; the similarity scaling gives a nominally linear profile where v decays as $1/y$. The ODT simulation compares very well with the stationary wire data in [19] after an initial induction period for $y/D < 20$. The dashed line in the plot is the linear curve fit reported by Hussein et

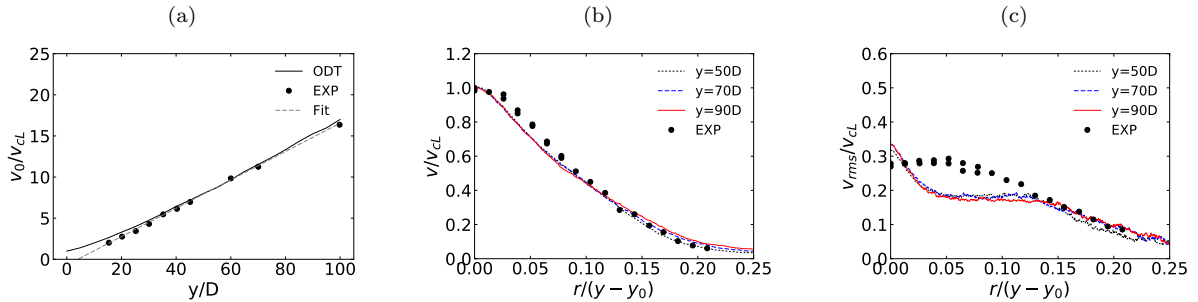


Fig. 8 Round jet results for TMA: (a) mean axial velocity along the centerline versus downstream location; (b) radial profiles of mean axial velocity at three downstream locations; (c) root mean square (RMS) radial profiles of streamwise velocity at three downstream locations.

al. Figure 7(b) shows radial profiles of the mean axial velocity normalized by the local centerline value. Profiles at three axial locations, $50D$, $70D$, and $90D$, are shown. The experimental data points shown are the laser Doppler anemometer (LDA) data in [19]. The ODT results show a similarity collapse of the data at $r/(y-y_0) < 0.1$, but some spread in the profiles at higher $r/(y-y_0)$, with the simulation results relaxing towards the experimental values with downstream distance. Figure 7(c) shows radial profiles of the axial root mean square (RMS) velocity normalized by the local centerline velocity at the same three positions. Here again, the profiles tend to relax towards the experimental (LDA) data at higher $r/(y-y_0)$ with downstream distance.

The quantitative agreement of v_{rms} velocity is generally good, especially for $r/(y-y_0) > 0.03$. At lower values, near the centerline, the ODT v_{rms} increases, whereas the experimental data decrease slightly. We attribute this to the so-called *centerline anomaly* of the cylindrical ODT formulation due to the geometric stretching associated with the cylindrical triplet maps. This stretching was shown in Figs. 2 and 3. In fact, the motivation for developing TMB was to minimize the degree of this geometric stretching. The stretching effect was present for both maps TMA and TMB, but it is largest near the centerline, where curvature is large. With increasing distance from the centerline, that is, for large distances compared to the eddy size, the geometric stretching effect becomes negligible for both maps, and they both approach the planar limit.

For comparison to the ODT results with TMB shown in Fig. 7, similar simulations were performed with TMA, and corresponding results are shown in Fig. 8. Here, β_{les} and Z are the same as for the previous case with TMB, but $C = 7$. Again, we see good agreement for the centerline velocity decay in Fig. 8(a). A somewhat better similarity collapse than for TMB occurs in the radial velocity profiles, though they are slightly lower than the experimental data at $r/(y-y_0) < 0.13$ and slightly higher than the experimental data at $r/(y-y_0) > 0.13$. The v_{rms} profiles also show strong similarity scaling. Compared with TMB, however, the simulations show a much higher centerline anomaly, and the v_{rms} profile departs from the experiments much further from the centerline and has a higher rise in the region $r/(y-y_0) < 0.05$.

It is worth noting that the v_{rms} profile depends somewhat on the ODT parameters selected. Hewson and Kerstein [15] demonstrated that mean centerline values of mixture fraction were insensitive to C and β_{les} provided their ratio was kept constant. In these simulations, however, higher values of RMS fluctuations were observed at lower values of β_{les} . Figure 9 shows results for TMA similar to those in Fig. 8 with varying C and β_{les} . Each of the three cases has $C/\beta_{les} = 2$, with $C = 7, 5,$ and 3 . Plots (b) and (c) show axial location $70D$. There is very little variation of the mean centerline velocity decay for the three cases. The radial profiles of the mean streamwise velocity are also very close, but they decrease somewhat in value with decreasing C for intermediate $r/(y-y_0)$ values. In contrast, the v_{rms} profiles are strongly dependent on the values of C and β_{les} for a constant C/β_{les} ratio, with increasing v_{rms} for decreasing β_{les} . These results are consistent with those presented for mixture fraction by Hewson and Kerstein [15]. In Fig. 9(c), the centerline anomaly appears to increase with decreasing β_{les} , and the departure from the data occurs further from the origin with increasing β_{les} . That is, the simulations fit more of the data over a wider radial range at lower values of β_{les} .

The centerline anomaly tends to increase the velocity fluctuations near the centerline. This is primarily due to the effect of the cylindrical triplet maps on the eddy rate, as shown in Fig. 5. To minimize the effect of the centerline anomaly, the planar evaluation of τ_e^{-1} described in Sec. 2.2.4 (PTMB) is used. Results are shown in Fig. 10. Here, $C = 7$, $\beta_{les} = 3.5$, and $Z = 400$. The centerline velocity decay and radial

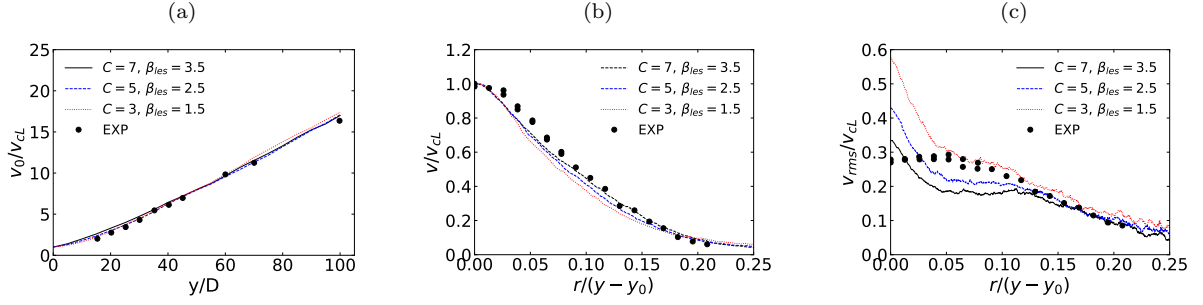


Fig. 9 Round jet results for TMA for three cases: (a) mean axial velocity along the centerline versus downstream location; (b) radial profiles of mean axial velocity at $y = 70D$; (c) root mean square (RMS) radial profiles of streamwise velocity $y = 70D$.

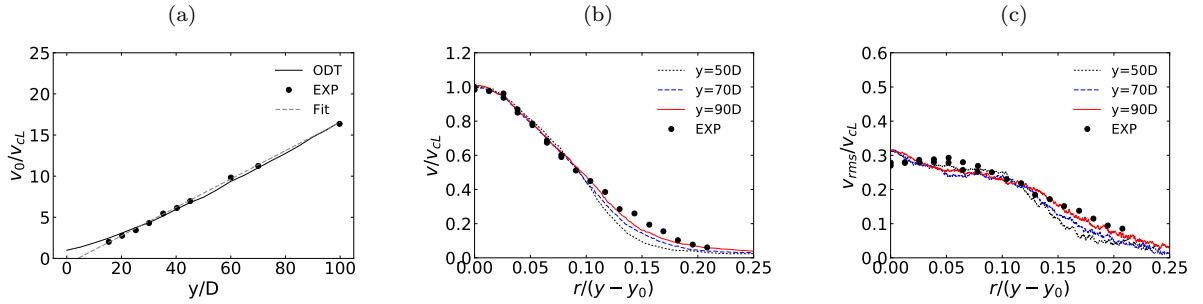


Fig. 10 Round jet results for the case of planar evaluation of τ_e^{-1} (PTMB): (a) mean axial velocity along the centerline versus downstream location; (b) radial profiles of mean axial velocity at three downstream locations; (c) root mean square (RMS) radial profiles of streamwise velocity at three downstream locations.

profiles show good agreement, as with the previous cases, with a slight improvement in the radial velocity profile. The v_{rms} profiles are significantly improved along the centerline compared to TMA and TMB. The centerline anomaly is not completely removed, however, since implemented eddies are still subject to the geometric distortion of the TMB map, whose influence is felt by the τ_e^{-1} calculation for subsequent eddy events.

3.3 Round jet flame

The new cylindrical ODT formulation is demonstrated in a round, reacting, turbulent jet flame. Results are compared to the experimental DLR-A flame of Meier et al. [37,1]. Heat release and temperature- and composition-dependent transport and thermodynamic properties are key characteristics of this flow. This canonical flame configuration has been used extensively to study and validate turbulent combustion models. Pitsch [42] studied differential diffusion effects in this flame using a classical unsteady flamelet model. Lindstedt and Ozarivsky [35] investigated it using a joint PDF approach, while Wang and Pope [53] used an LES/PDF model combined with a flamelet/progress-variable (FPV) model. Fairweather and Woolley [11] studied several chemical mechanisms using the DLR flame and a first order conditional moment closure (CMC) model, and Lee and Choi [30,29] studied NO emissions using an Eulerian particle flamelet model. These studies consisted of computational fluid dynamics (CFD) simulations with subgrid modeling of the turbulent combustion process. In contrast, ODT is a low-dimensional representation of the entire flow, not just the subgrid scales. Previous ODT studies of turbulent jet flames have employed the temporal planar formulation, so we expect that the model may improve with a spatial cylindrical formulation that more closely matches the experimental configuration.

The DLR-A fuel stream is mixture of 22.1% CH₄, 33.2% H₂, and 44.7% N₂ (by volume) that issues into dry air. The fuel stream exits a nozzle with an inner diameter of 8 mm at a mean exit velocity of 42.2

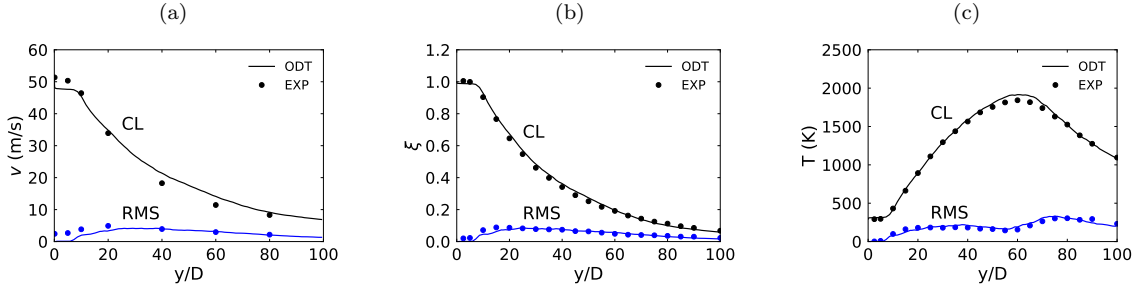


Fig. 11 DLR jet flame results for TMB: (a) mean axial velocity and RMS velocity along the centerline versus downstream location; (b) mean axial mixture fraction and RMS mixture fraction along the centerline versus downstream location; (c) mean axial temperature (K) and RMS temperature (K) along the centerline versus downstream location.

ms^{-1} . The coflowing air stream issues from a nozzle of diameter 140 mm at a velocity of 0.3 ms^{-1} . The reported Reynolds number is 15,200.

The ODT simulation uses these diameters and the experimentally reported velocity profile at the jet exit. Whereas in the nonreacting case, a small velocity was added uniformly to the profile, no velocity addition is needed here because of the slow-moving coflow air stream present alongside the reacting jet. The ODT simulation includes the buoyant source term but not the streamwise pressure gradient in Eq. (25). The fuel was diluted with N_2 in the experimental flame to minimize radiative heat losses, and radiation is ignored in the simulation. This flame has a low Reynolds number and the combustion chemistry proceeds quickly. The ODT simulation transports the following species: O_2 , N_2 , CH_4 , H_2 , H_2O , CO_2 . Reactions are assumed to proceed to products of complete combustion:



and simple, fast reaction rates are applied. These assumptions are not reasonable for the DLR-A flame. The primary purpose of these simulations is to illustrate ODT in a reacting jet with variable properties and heat release.

ODT simulations were performed using the TMB triplet map with parameters $C = 20$, $\beta_{les} = 17$, and $Z = 400$. The values of C and β_{les} were adjusted to give good agreement of the jet evolution with the experimental data, while the value of Z was taken as the same value as for the jet in Sec. 3.2. Results of the simulation are presented in Figs. 11 and 12. 1000 independent flow realizations were performed and the results ensemble averaged. Downstream distance y , and radial position r are normalized by the jet diameter D .

Figure 11 shows ODT and experimental axial mean and RMS profiles along the jet centerline for (a) axial velocity, (b) mixture fraction ξ , and (c) temperature T . The ODT results track the experimental data well for all three variables. The centerline temperature is about 100 K above the experiments at the peak at $y/D = 60$. This small difference is likely due to thermal radiation and differences between equilibrium products and products of complete combustion.

The centerline velocity has a fast initial decrease due to diffusion. There is a delay in the ODT RMS profiles on the centerline before the eddies occur near $y/D = 7$. This delay is due to the elapsed time model for large eddy suppression discussed in Sec. 2.2.2 so that, initially, only small eddies occur in the shear layers on the jet edges away from the centerline. The experimental RMS measurements also reflect non-vortical “flapping” of the jet [13, 4] that ODT is not able to capture. Centerline RMS agreement is good for all variables for $y/D > 25$. Note especially that the ODT captures the dip in the RMS temperature profile near the peak temperature at $y/D = 60$. This decrease in the RMS fluctuations is due to the combined effects of decreased density and increased viscosity at high temperature, which decrease the local Reynolds number.

Radial profiles of mean mixture fraction and temperature for the jet are shown in Fig. 12 at six downstream locations. The ODT and experimental profile widths are in good agreement, with the ODT being slightly narrower. The peak temperature values in the “wings” occur at the flame surfaces, and the ODT values overpredict the experiments. This could be due to radiative losses and finite-rate chemistry effects, which are not modeled here.

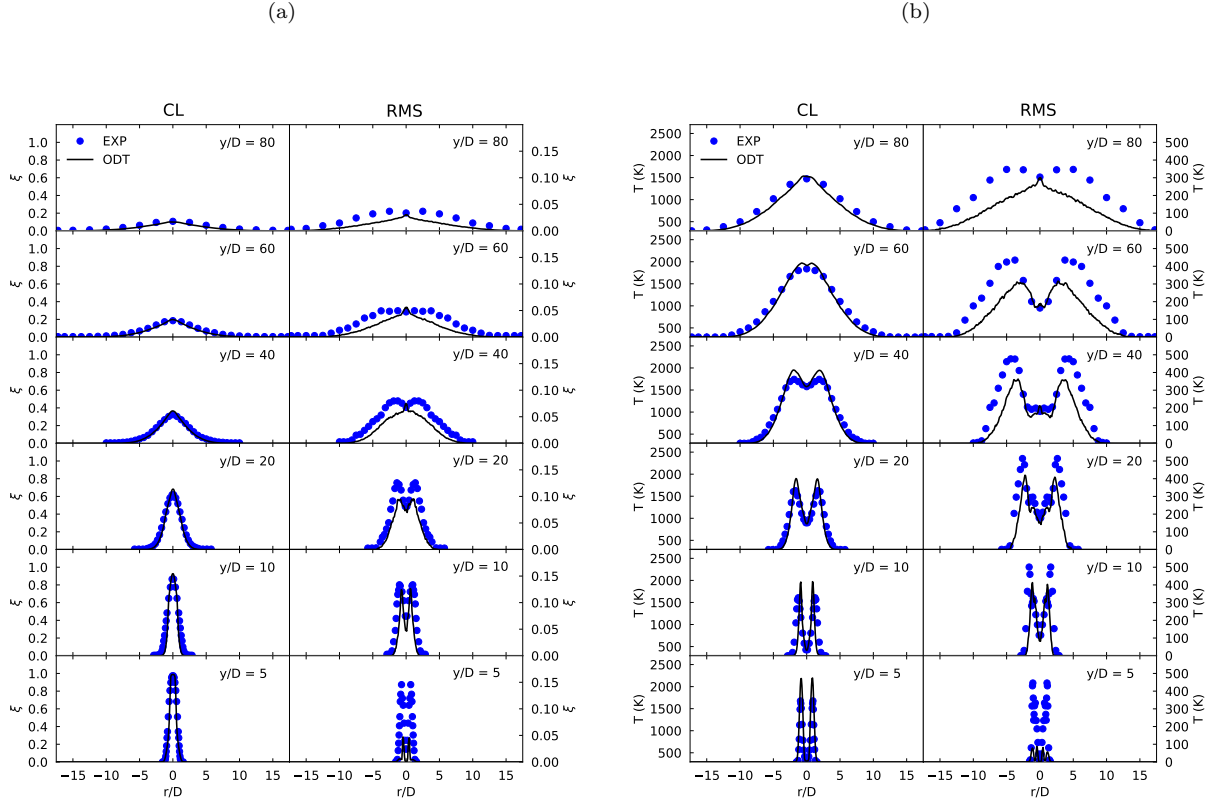


Fig. 12 Radial mean and RMS profiles for mixture fraction (a) and temperature (b) for the DLR jet flame.

The RMS temperature and mixture fraction profiles are also shown in Fig. 12. While the fluctuations are accurate on the centerline, the ODT underpredict the experiments away from the centerline. This depends on the ODT parameters chosen, as shown in Fig. 9. The very large difference in the RMS profiles at low y/D is simply due to the delay in the ODT eddies noted previously and the possible flapping contribution that ODT does not capture. The centerline anomaly can also be seen in the RMS profiles for $y/D \geq 40$, but the magnitude is somewhat smaller than was observed in the nonreacting jet simulations.

Simulations were also performed using the PTMB model. Optimal parameters were close to those for the TMB case: $C = 18$, $\beta_{les} = 18$, and $Z = 400$. The results are so similar to the TMB case that we do not include them here. As expected, the centerline anomaly is decreased, consistent with the behavior of the nonreacting jet, shown previously.

The difference in the optimal parameters for the reacting and nonreacting jets for the TMB model are surprising. Z is the same for both simulations, but $C = 5.25$, $\beta_{les} = 3.5$, $C/\beta_{les} = 1.5$ for the nonreacting jet, and $C = 20$, $\beta_{les} = 17$, $C/\beta_{les} = 1.18$ for the DLR-A flame. Both jets had reasonably good agreement with the experiments. We ran the DLR-A flame with the nonreacting jet parameters. The results for the centerline mixture fraction are shown in Fig. 13. The nonreacting parameters result in faster centerline decay and higher RMS velocity fluctuations.

Differences in the required parameters for the reacting jet may be expected due to effects of variable density and viscosity. However, we expect flow dilatation to have a significant impact. Hewson and Kerstein [15] discussed the effect of flow dilatation on ODT evolution in some detail and the results we observe here are consistent with their analysis. In ODT, flow dilatation occurs only in the radial direction and directly affects only flow length scales. Real dilatation at low Mach numbers is three dimensional, and affects both length scales and velocity, with the effects of increasing rates of dissipation (which scale as u^3/l), and pushing the flow downstream. This is seen in Fig. 13, where the centerline experimental mixture fractions fall off more slowly than for ODT with the nonreacting parameter values. This is counteracted in ODT with a lower C/β_{les} ratio, effectively reducing the mixing rate and shifting the ODT mixture fraction curve

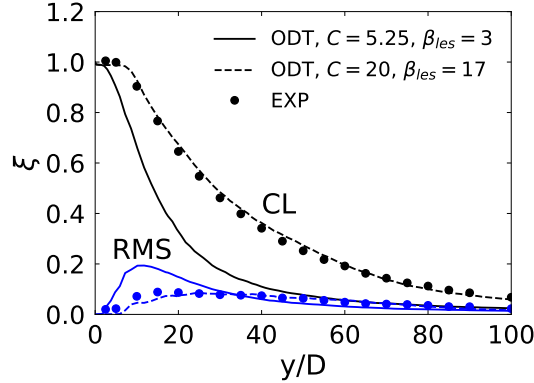


Fig. 13 Centerline mean and RMS mixture fraction for the DLR-A flame with nonreacting jet parameters, and optimized parameters.

downstream. Figure 9 showed that RMS fluctuations were lower for higher values of C for a given C/β_{les} ratio. Hence, the higher C value used in the tuned DLR-A case also tends to reduce the high RMS values seen in Fig. 13 at $y/D < 35$.

4 Conclusions

A new formulation of the ODT model in cylindrical and spherical coordinates was developed and presented. A Lagrangian finite-volume method utilizing an adaptive mesh was used, and the model is formulated for both temporal and spatial variants.

ODT resolves a full range of length and time scales in a physical space coordinate. This unique aspect of the model allows high fidelity investigation into a wide range of complex multi-scale turbulent flows. DNS is the only simulation approach that can resolve all continuum scales in three dimensions. But DNS is computationally expensive, limiting the number of simulations that can be performed and the accessible parameter space (e.g., the range of Reynolds numbers available). ODT can be used to study flows outside of the parameter space available to DNS, and is computationally efficient enough to allow extensive parametric study. However, ODT models turbulent advection, and is not able to directly capture multi-dimensional flow structures or transport. ODT also includes model parameters that must be adjusted for specific flows. Hence, ODT is most reliable when used in conjunction with experimental data, or when experimental data is used as a basis for calibrating ODT that is subsequently used in extrapolative studies.

Previous ODT simulations were limited to planar configurations, but many detailed experiments of turbulent flows, especially jets and jet flames, are axi-symmetric (cylindrical). While temporal planar ODT can be reasonably applied to cylindrical jets due to similar scaling behaviors, this is not ideal due to differences in implied fluid time-history profiles (important for particle studies, soot formation, and flame-extinction/reignition, for example), and geometric effects, such as obtaining correct mass flow rates in piloted flames. Improved consistency in the geometric configuration between ODT and experiments reduces uncertainties in the source of discrepancies.

The cylindrical and spherical formulations were presented for the unsteady evolution equations of mass, momentum, energy and species. Some extensions and corrections to the treatment of constrained volume flows with variable density in [33] were given. For flows with dilatation, while planar flows allow the center of the fluid expansion to be fixed, in cylindrical and spherical flows we fix the radial origin.

Turbulent advection is modeled as instantaneous eddy events implemented using the triplet map. In cylindrical and spherical coordinates, geometric stretching occurs in the three map images. Two triplet map variants were presented, TMA and TMB. In TMA, each map segment has the same volume, resulting in each segment having different radial lengths. In TMB, each map segment is given the same radial segment length, resulting segments having different volumes. The geometric stretching is strongest near the origin and is due to the volume dependence on radial location. The stretching affects the eddy timescale, resulting in a so-called centerline anomaly, that was manifested as an increase in velocity fluctuations near

the centerline in the jet configuration studied. The TMB map performed better than TMA. A hybrid planar-TMB (PTMB) map was also presented and this further reduced the centerline anomaly.

Three flow configurations were studied: a temporal pipe flow, a spatial nonreacting jet at high Reynolds number, and a spatial reacting jet flame at relatively low Reynolds number. The jet flame illustrates effects of variable density and viscosity, including dilatational effects, which had a significant impact on the required ODT parameters. The cylindrical ODT formulation was found to capture key features of DNS results for pipe flow, and experimental results were reproduced with quantitative accuracy in most instances for the nonreacting and reacting jets, which are considered to be an improvement over previous temporal formulations, though this is not explicitly investigated here. The TMA, TMB, and PTMB maps gave nearly identical results for the pipe flow, where the key dynamics are near-wall away from the centerline where stretching effects are important. The ODT C and Z parameters were nearly the same for the jet (TMB) and the pipe flow, illustrating a degree of robustness of the ODT parameters across configurations.

While spherical ODT was formulated here, the focus was on cylindrical flows. Application of ODT to spherical flows, will be the subject of future study. The brief pipe flow results presented here were used for illustration. A more comprehensive and detailed study of pipe flow is underway [36], that includes the spatial and temporal ODT formulations, and analysis of turbulent kinetic energy budgets. Further applications of the cylindrical ODT formulation to jet flames are also underway.

Appendix A: ODT time advancement procedure

The overall advancement scheme for temporal ODT is outlined here, including some algorithmic details related to the time advancement. Formally, the outcome of time advancement of any property c from time $t = 0$ to time t^* can be expressed as

$$c(x, t) = T[t_n, t^*]E(x_n, l_n) \cdots T[t_j, t_{j+1}]E(x_j, l_j)T[t_{j-1}, t_j] \cdots E(x_2, l_2)T[t_1, t_2]E(x_1, l_1)T[0, t_1]c(x, 0), \quad (40)$$

where capital letters represent operators. $T[t_{j-1}, t_j]$ denotes time advancement of $c(x, t_{j-1})$ from t_{j-1} to t_j . The equations governing the advancement of the flow and state properties included in present formulation are shown in Sec. 2.3. $E(x_j, l_j)$ denotes an eddy event that induces an instantaneous change $c(x, t_j) \rightarrow c'(x, t_j)$, where x_j is the left edge of the j^{th} eddy, l_j is its length, and t_j is its time of occurrence. The procedure for sampling these eddy attributes is described below. n is the number of eddy events that occur during $[0, t^*]$.

A key feature of the sampling procedure is that it samples candidate events that are then subject to acceptance or rejection based on a computed acceptance probability P_a . Before explaining these details, we note their consequences with regard to the sequence of operations shown in Eq. (40).

Equation (40) represents the operations that can modify property c . Candidate events that are rejected have no such effect, so they are not included in that representation. The numerical algorithm therefore requires a more detailed representation. The arguments of T and E can now be omitted for brevity; the full notation can be inferred from Eq. (40). Denoting a rejected candidate event by R , a representative sequence of operations during some subinterval of a simulated realization can be expressed as

$$\cdots TRTRTETRTRTRTRTRTETRTRTRT \cdots$$

The greater frequency of rejections than acceptances is intended to illustrate the smallness of P_a , which is explained below.

The time interval between candidate events (R or E) is extremely small for two reasons. First, under typical conditions, the time between eddies containing a given location is comparable to the diffusion time scale that corresponds to the typical eddy size. The smallest (Kolmogorov) eddies are the most numerous and hence the typical eddies. Due to their smallness, many of them must occur during some time interval in order for a given location to be contained in one of them. This implies that the time between eddies is much smaller than the diffusion time scale, which, by the same reasoning, is roughly the Kolmogorov time scale, assuming gas-phase conditions.

Second, these considerations apply to the physically occurring (accepted) eddies. As noted, rejected candidate eddies are much more frequent, so the time interval between them is commensurately smaller. Therefore, the T operation in the above advancement representation typically acts over a time interval much smaller than the maximum permitted by accuracy and stability constraints, which is grossly inefficient.

To remedy this, recall that the event R causes no change of the system state, hence its omission from Eq. (40). Therefore, the occurrence of such an event need not trigger an advancement operation if that

operation is not otherwise needed. Restoring a somewhat fuller notation with indices labeling successive time epochs and intervals, a representative simulated realization is then

$$c(x, t) = \cdots T_{5,9} E_9 R_8 R_7 R_6 T_{0,5} E_5 R_4 R_3 R_2 R_1 c(x, 0). \quad (41)$$

In this example, E_5 is implemented before the system advancement from time 0 to time t_5 , and likewise E_9 is implemented before the system advancement from time t_5 to time t_9 . This is unavoidable because eddy occurrences are unknown until an eddy trial is performed. The outcome of a trial depends on the system state, so it would be inconsistent to accept an eddy and then update the prior system state (by applying, e.g., the operator $T_{0,5}$ or $T_{5,9}$) followed by implementation of the eddy. (This could induce, among other things, violations of energy conservation.) Thus, the time advancement is lagged relative to the eddy sampling and implementation but catches up immediately after each implemented eddy event.

For this reversal of operator sequencing relative to Eq. (40) to be valid, the time interval between T operations must be small enough that the error resulting from basing an eddy trial on the system state at an earlier time is negligible in terms of the sensitivity of relevant output statistics to this error. To enforce this insensitivity, an accuracy criterion is used after each rejection of a candidate eddy to decide whether to do an advancement catch-up. This might result in, e.g., an added T operation after eddy rejection R_7 in Eq. (41), and thus

$$c(x, t) = \cdots T_{7,9} E_9 R_8 T_{5,7} R_7 R_6 T_{0,5} E_5 R_4 R_3 R_2 R_1 c(x, 0). \quad (42)$$

The scheme illustrated by Eq. (42) has proven to be accurate and efficient for the present as well as previous ODT formulations and is the basis of the computations reported here.

The difference between the implemented numerical scheme and the formal representation of ODT time advancement, Eq. 40, is largely a consequence of the aforementioned eddy sampling procedure. As noted in Sec. 2.2.2, this procedure is needed because the eddy rate distribution $\lambda_e(x_0, l)$ depends on the entire system state and is thus continually evolving. Direct sampling from this distribution would therefore require its continual reconstruction, which is unaffordable. Instead, the implemented approach involves sampling from a fixed distribution that is necessarily incorrect followed by an acceptance trial that corrects the resulting sampling bias using only an evaluation of λ_e for the particular eddy that is sampled.

This approach involves aspects of the rejection method [41] and the thinning method [31]. In the thinning method, we sample eddy times as a Poisson process with mean rate $1/\Delta t_s$, where the mean eddy sampling interval Δt_s is chosen to be small enough so that the sampling rate always exceeds the unknown, time-varying aggregate rate Λ of all eddy events. These sampled eddies would be accepted with probability $P_{a,t} = \Lambda \Delta t_s$, but $P_{a,t}$ is unknown because Λ is unknown. This relation is nevertheless useful in combination with other information, as follows. In the rejection method, we replace the unknown joint probability density function (PDF) $P(x_0, l)$ with a specified PDF $\hat{P}(x_0, l)$. We sample eddy positions and sizes from $\hat{P}(x_0, l)$. This allows a relative acceptance weighting $W_{a,r} = C P(x_0, l) / \hat{P}(x_0, l)$ to be defined, where the coefficient C is not yet determined. Multiplication of $P_{a,t}$ by $W_{a,r}$ gives an acceptance rate P_a that is proportional to the true rate $\lambda_e(x_0, l) dx_0 dl = \Lambda P(x_0, l) dx_0 dl$ of occurrence of eddies with parameter values within the ranges $[x_0, x_0 + dx]$ and $[l, l + dl]$, respectively. Hence,

$$P_a = C \frac{\lambda_e \Delta t_s}{\hat{P}(x_0, l)} \quad (43)$$

for some fixed value of C . As explained in in Sec. 2.2.2, the true value λ_e is evaluated for the candidate eddy as $1/(\tau_e l^2)$

To evaluate C , first note that the above procedure can be generalized from the differential elements $[x_0, x_0 + dx]$ and $[l, l + dl]$ to any subset of the possible values of x_0 and l , and hence to their complete ranges. Then the denominator in Eq. (43) is replaced by the integral of $\hat{P}(x_0, l)$ over the full range of its arguments, which is unity based on PDF normalization, and, by definition, λ_e in the numerator is replaced by Λ . This reduces Eq. (43) to $P_a = C \Lambda \Delta t_s$, where the true value Λ would be very costly to evaluate, though this could in principle be done. The point here, however, is that $C = 1$ recovers the aforementioned thinning result, thus finally establishing that

$$P_a = \frac{\hat{\lambda}_e \Delta t_s}{\hat{P}(x_0, l)}. \quad (44)$$

$\hat{P}(x_0, l)$ is taken to be

$$\hat{P}(x_0, l) = g(x_0) f(l). \quad (45)$$

$g(x_0)$ is a uniform distribution over the range $[0, L_d - l]$, where L_d is the domain length. Its dependence on l indicates that l must be sampled before x_0 . (The range is $[0, L]$ for the case of periodic boundary conditions.) $f(l)$ is taken to be

$$f(l) = \frac{A_{\tilde{l}}}{l^2} e^{-2\tilde{l}/l}, \quad (46)$$

where \tilde{l} is the most probable eddy size, as specified by the user, and $A_{\tilde{l}}$ is the PDF normalization constant.

To summarize, we sample an eddy position x_0 and size l from $\hat{P}(x_0, l)$ at an eddy occurrence time evaluated from a Poisson process with mean rate $1/\Delta t_s$ and accept that eddy with the probability given in Eq. (44). Δt_s is adjusted during the simulation to ensure that P_a is always less than unity. The rejection and thinning methods affect the eddy sampling efficiency, but not the accuracy of the process. The closer P_a is to unity, and the better the approximation $\hat{P} \approx P$, the more efficient the method will be. However, the possible system states during a typical realization are so diverse that P_a varies widely for given Δt_s , so to ensure that $P_a < 1$, Δt_s has to be small enough that P_a is typically very small. As noted above, this has ramifications with regard to the design of the time advancement scheme. In any case, this approach is much faster than directly sampling $P(x_0, l)$, which would require it to be continually updated.

Appendix B: Pressure term in the energy equation

The pressure term in Eq. (27) arises in constant or constrained volume ideal gas flows. That term was derived in [33] for planar flows; the treatment here is similar, but with some extensions and minor corrections. We constrain ourselves to a low-Mach number formulation [44]. The pressure term is then

$$\frac{dP}{dt} = -\gamma P \nabla \cdot \mathbf{u} + \gamma P \mathcal{U}. \quad (47)$$

Here, $\gamma = c_p/c_v = c_p/(c_p - R/M)$, where c_p and c_v are heat capacities (per unit mass), R is the universal gas constant, M is the mean molecular weight, and \mathcal{U} is

$$\mathcal{U} = \frac{1}{\rho c_p T} \left(-\nabla \cdot \mathbf{q} + \sum_k h_k (\nabla \cdot \mathbf{j}_k - \dot{m}_k''') \right) - \frac{M}{\rho} \sum_k \frac{1}{M_k} (\nabla \cdot \mathbf{j}_k - \dot{m}_k'''). \quad (48)$$

In this equation, h_k is the enthalpy of species k per unit mass. Equation (47) is integrated over the whole domain by assuming that P and dP/dt are spatially uniform. This gives

$$\frac{dP}{dt} = \frac{\int \mathcal{U} dV - (U_{Rbc} A_{Rbc} - U_{Lbc} A_{Lbc})}{\frac{1}{P} \int \frac{1}{\gamma} dV}. \quad (49)$$

Here, U_{Rbc} and U_{Lbc} denote velocities of the right and left boundaries; they are normally zero for constant volume configurations but are retained here for generality. The volume integrals extend over the whole domain and are evaluated as a summation over cell integrals. See also Eq. (51) below. As before, we assume that cells have uniform properties.

Given dP/dt , we compute the dilatational cell face velocities for use in the Lagrangian formulation for constant or constrained volume flows. Equation (47) is solved for $\nabla \cdot \mathbf{u}$ and volume integrated over an individual cell to give an expression for the difference between cell face velocities:

$$U_e A_e - U_w A_w = -\frac{1}{\gamma P} \frac{dP}{dt} V + \int \mathcal{U} dV, \quad (50)$$

$$\int \mathcal{U} dV = \frac{1}{\rho c_p T} \left(-(q_e A_e - q_w A_w) + \sum_k h_k (j_{k,e} A_e - j_{k,w} A_w - \dot{m}_k''' V) \right) - \frac{M}{\rho} \sum_k \frac{1}{M_k} (j_{k,e} A_e - j_{k,w} A_w - \dot{m}_k''' V). \quad (51)$$

In the evaluation of Eqs. (50, 51), the volume integrals of the divergences of vector quantities were converted to surface integrals using the Gauss Divergence Theorem; that way, the equations use readily available cell face velocities and fluxes. Using Eqs. (50, 51), any given face velocity can be computed by marching from a known boundary velocity.

While dP/dt given in Eq. (49) is used in Eqs. (50, 27), the pressure itself is updated following Motheau and Abraham [40], where the pressure is set by the global gas state using the ideal gas law. The mass on the line is given by $m_l = \int \rho dV$, where $\rho = MP/(RT)$. When P is spatially uniform, we obtain

$$P = \frac{m_l R}{\int \frac{M}{T} dV}. \quad (52)$$

Acknowledgements This work was supported by the National Science Foundation under grant number CBET-1403403.

References

1. International workshop on measurement and computation of turbulent nonpremixed flames, URL: <http://www.sandia.gov/TNF/DataArch/DLRflames.html>
2. Ashurst, W.T., Kerstein, A.R.: One-dimensional turbulence: Variable-density formulation and application to mixing layers. *Physics of Fluids* **17**, 025,107 (2005)
3. Ashurst, W.T., Kerstein, A.R.: Erratum: One-dimensional turbulence: variable density formulation and application to mixing layers. *Physics of Fluids* **21-119901**, 1 (2009)
4. Binder, G., Favre-Marinet, M.: Some characteristics of pulsating or flapping jets. In: R. Michel, J. Cousteix, R. Houdeville (eds.) *Unsteady turbulent shear flows*, pp. 370–379. Springer (1981)
5. Cao, S., Echekki, T.: A low-dimensional stochastic closure model for combustion large-eddy simulation. *Journal of Turbulence* **9**, 1–35 (2008)
6. Cengel, Y.A., Cimbala, J.M.: *Fluid Mechanics*, 2 edn. McGraw-Hill (2006)
7. Chin, C., Monty, J.P., Ooi, A.: Reynolds number effects in DNS of pipe flow and comparison with channels and boundary layers. *Int. J. Heat Fluid Flow* **45**, 33–40 (2014)
8. Cohen, S.D., Hindmarsh, A.C.: CVODE, a stiff/nonstiff ODE solver in C. *Computational Physics* **10**, 138–143 (1996). <http://llnl.gov/casc/sundials/>
9. Cook, A.W., Riley, J.J., Kosaly, G.: A laminar flamelet approach to subgrid-scale chemistry in turbulent flows. *Combustion and Flame* **109**, 332–341 (1997)
10. Echekki, T., Kerstein, A.R., Dreeben, T.D.: One-dimensional turbulence simulation of turbulent jet diffusion flames: Model formulation and illustrative applications. *Combustion and Flame* **125**, 1083–1105 (2001)
11. Fairweather, M., Woolley, R.: First-order conditional moment closure modeling of turbulent, nonpremixed methane flames. *Combustion and Flame* **138**, 3–19 (2004)
12. Gastine, T., Wicht, J., Aurnou, J.M.: Turbulent Rayleigh-Benard convection in spherical shells. *Journal of Fluid Mechanics* **778**, 721–764 (2015)
13. Goldschmidt, V.W., Bradshaw, P.: Flapping of a plane jet. *Physics of Fluids* **16**, 354–355 (1973)
14. Goshayeshi, B., Sutherland, J.C.: Prediction of oxy-coal flame stand-off using high-fidelity thermochemical models and the one-dimensional turbulence model. *Proceedings of the Combustion Institute* **35**, 2829–2837 (2015)
15. Hewson, J.C., Kerstein, A.R.: Stochastic simulation of transport and chemical kinetics in turbulent CO/H₂/N₂ flames. *Combustion Theory and Modelling* **5**, 669–697 (2001)
16. Hewson, J.C., Kerstein, A.R.: Local extinction and reignition in nonpremixed turbulent CO/H₂/N₂ jet flames. *Combustion Science and Technology* **174**, 35–66 (2002)
17. Hewson, J.C., Ricks, A.J., Tieszen, S.R., Kerstein, A.R., Fox, R.O.: Conditional moment closure with differential diffusion for soot evolution in fire. In: *Center for Turbulence Research, Proceedings of the Summer Program* (2006)
18. Hewson, J.C., Ricks, A.J., Tieszen, S.R., Kerstein, A.R., Fox, R.O.: On the transport of soot relative to a flame: modeling differential diffusion for soot evolution in fire. In: H. Bockhorn, A. D’Anna, A.F. Sarofim, H. Wang (eds.) *Combustion Generated Fine Carbonaceous Particles*. KIT Scientific Publishing (2009)
19. Hussein, H.J., Capp, S.P., George, W.K.: Velocity measurements in a high-Reynolds-number, momentum-conserving, axisymmetric, turbulent jet. *Journal of Fluid Mechanics* **258**, 31–75 (1994)
20. Jozefik, Z., Kerstein, A.R., Schmidt, H.: Simulation of shock-turbulence interaction in non-reactive flow and in turbulent deflagration and detonation regimes using one-dimensional turbulence. *Combustion and Flame* **164**, 53–67 (2016)
21. Jozefik, Z., Kerstein, A.R., Schmidt, H., Lyra, S., Kolla, H., Chen, J.H.: One-dimensional turbulence modeling of a turbulent counterflow flame with comparison to DNS. *Combustion and Flame* **162**, 2999–3015 (2015)
22. Kerstein, A.R.: Linear-eddy modelling of turbulent transport. Part 6. Microstructure of diffusive scalar mixing fields. *Journal of Fluid Mechanics* **231**, 361–394 (1991)
23. Kerstein, A.R.: One-dimensional turbulence: Model formulation and application to homogeneous turbulence, shear flows, and buoyant stratified flows. *Journal of Fluid Mechanics* **392**, 277–334 (1999)
24. Kerstein, A.R., Ashurst, W.T., Wunsch, S., Nilsen, V.: One-dimensional turbulence: Vector formulation and application to free shear flows. *Journal of Fluid Mechanics* **447**, 85–109 (2001)
25. Kerstein, A.R., Dreeben, T.D.: Prediction of turbulent free shear flow statistics using a simple stochastic model. *Physics of Fluids* **12**, 418–424 (2000)
26. Houry, G., Schlatter, P., Noorani, A., Fischer, P., Brethouwer, G., Johansson, A.: Direct numerical simulation of turbulent pipe flow at moderately high Reynolds numbers. *Flow Turbulence Combust.* **91**, 475–495 (2013)
27. Krishnamoorthy, N.: Reaction models and reaction state parameterization for turbulent nonpremixed combustion. Ph.D. thesis, The University of Utah (2008)
28. Lackmann, T., Kerstein, A.R., Oevermann, M.: A representative linear eddy model for simulating spray combustion in engines. Submitted to *Combustion and Flame*, 2017
29. Lee, K., Choi, D.: Analysis of NO formation in high temperature diluted air combustion in a coaxial jet flame using an unsteady flamelet model. *International Journal of Heat and Mass Transfer* **52**, 1412–1420 (2009)

30. Lee, K.W., Choi, D.H.: Prediction of NO in turbulent diffusion flames using eulerian particle flamelet model. *Combustion Theory and Modelling* **12**, 905–927 (2008)
31. Lewis, P.A., Shedler, G.S.: Simulation of nonhomogeneous poisson processes by thinning. *Naval Res. Logistics Quart.* **26**, 403–413 (1979)
32. Lignell, D.O., Fredline, G.C., Lewis, A.D.: Comparison of one-dimensional turbulence and direct numerical simulations of soot formation and transport in a nonpremixed ethylene jet flame. *Proceedings of the Combustion Institute* **35**, 1199–1206 (2015)
33. Lignell, D.O., Kerstein, A.R., Sun, G., Monson, E.I.: Mesh adaption for efficient multiscale implementation of one-dimensional turbulence. *Theoretical and Computational Fluid Dynamics* **27**, 273–295 (2013)
34. Lignell, D.O., Rappleye, D.: One-dimensional-turbulence simulation of flame extinction and reignition in planar ethylene jet flames. *Combustion and Flame* **159**, 2930–2943 (2012)
35. Lindstedt, R., Ozarovsky, H.: Joint scalar transported PDF modeling of nonpiloted turbulent diffusion flames. *Combustion and Flame* **143**, 471–490 (2005)
36. Medina, J., Schmidt, H., Lignell, D.O.: Application of one-dimensional turbulence to incompressible channel and pipe flow . Submitted to *Journal of Turbulence*, (2017).
37. Meier, W., Barlow, R., Chen, Y.L., Chen, J.Y.: Raman/Rayleigh/LIF measurements in a turbulent CH₄/H₂/N₂ jet diffusion flame: experimental techniques and turbulence-chemistry interaction. *Combustion and Flame* **123**, 326–343 (2000)
38. Meiselbach, F.: Application of ODT to turbulent flow problems. Ph.D. thesis, Brandenburgische Technische Universität Cottbus-Senftenberg (2015)
39. Monson, E.I., Lignell, D.O., Werner, C., Hintze, R.S., Finney, M.A., Jozefik, Z., Kerstein, A.R.: Simulation of ethylene wall fires using the spatially-evolving one-dimensional turbulence model. *Fire Science and Technology* **52**, 167–196 (2016)
40. Motheau, E., Abraham, J.: A high-order numerical algorithm for DNS of low-mach-number reactive flows with detailed chemistry and quasi-spectral accuracy. *Journal of Computational Physics* **313**, 430–454 (2016)
41. Papoulis, A., Pillai, S.U.: *Probability, Random Variables, and Stochastic Processes*, fourth edn. McGraw-Hill, New York (2002)
42. Pitsch, H.: Unsteady flamelet modeling of differential diffusion in turbulent jet diffusion flames. *Combustion and Flame* **123**, 358–374 (2000)
43. Punati, N., Sutherland, J.C., Kerstein, A.R., Hawkes, E.R., Chen, J.H.: An evaluation of the one-dimensional turbulence model: Comparison with direct numerical simulations of CO/H₂ jets with extinction and reignition. *Proceedings of the Combustion Institute* **33**, 1515–1522 (2011)
44. Rehm, R.G., Baum, H.R.: The equations of motion for thermally driven buoyant flows. *Journal of Research of the National Bureau of Standards* **83**, 297–308 (1978)
45. Ricks, A.J., Hewson, J.C., Kerstein, A.R., Gore, J.P., Tieszen, S.R., Ashurst, W.T.: A spatially developing one-dimensional turbulence (ODT) study of soot and enthalpy evolution in meter-scale buoyant turbulent flames. *Combustion Science and Technology* **182**, 60–101 (2010)
46. Schmidt, J.R., Wendt, J.O.L., Kerstein, A.R.: Non-equilibrium wall deposition of inertial particles in turbulent flow. *Journal of Statistical Physics* **137**, 233–257 (2009)
47. Schmidt, R.C., Kerstein, A.R., McDermott, R.: ODTLES: A multi-scale model for 3D turbulent flow based on one-dimensional turbulence modeling. *Computer Methods in Applied Mechanics and Engineering* **199**, 865–880 (2010)
48. Schmidt, R.C., Kerstein, A.R., Wunsch, S., Nilsen, V.: Near-wall LES closure based on one-dimensional turbulence modeling. *Journal of Computational Physics* **186**, 317–355 (2003)
49. Shihn, H., DesJardin, P.E.: Near-wall modeling for vertical wall fires using one-dimensional turbulence. In: *Proceedings of IMECE04 ASME International Mechanical Engineering Congress and Exposition*, Anaheim, CA (November 13–20, 2004)
50. Strang, G.: On the construction and comparison of difference schemes. *SIAM Journal of Numerical Analysis* **5**, 506–517 (1968)
51. Sun, G., Hewson, J.C., Lignell, D.O.: Evaluation of stochastic particle dispersion modeling in turbulent round jets. *International Journal of Multiphase Flow* **89**, 108–122 (2017)
52. Sun, G., Lignell, D.O., Hewson, J.C., Gin, C.R.: Particle dispersion in homogeneous turbulence using the one-dimensional turbulence model. *Physics of Fluids* **26**, 103,301 (2014)
53. Wang, H., Pope, S.B.: Large eddy simulation/probability density function modeling of a turbulent CH₄/H₂/N₂ jet flame. *Proceedings of the Combustion Institute* **33**, 1319–1330 (2011)
54. Wunsch, S., Kerstein, A.: A model for layer formation in stably stratified turbulence. *Physics of Fluids* **13**, 702–712 (2001)